


## Weakly Flux-Tunable Superconducting Qubit

José M. Chávez-García<sup>Ⓢ,†,‡</sup>, Firat Solgun<sup>Ⓢ,†</sup>, Jared B. Hertzberg<sup>Ⓢ</sup>, Oblesh Jinka<sup>Ⓢ</sup>, Markus Brink, and Baleegh Abdo<sup>Ⓢ,\*†</sup>

*IBM Quantum, IBM T. J. Watson Research Center, Yorktown Heights, New York 10598, USA*

 (Received 8 March 2022; revised 5 August 2022; accepted 5 August 2022; published 22 September 2022)

Flux-tunable qubits are a useful resource for superconducting quantum processors. They can be used to perform CPHASE gates, facilitate fast reset protocols, avoid qubit-frequency collisions in large processors, and enable certain fast readout schemes. However, flux-tunable qubits suffer from a trade-off between their tunability range and sensitivity to flux noise. Optimizing this trade-off is particularly relevant for enabling fast, high-fidelity, all-microwave cross-resonance gates in large, high-coherence processors. This is mainly because cross-resonance gates set stringent conditions on the frequency landscape of neighboring qubits, which are difficult to satisfy with nontunable transmons due to their relatively large fabrication imprecision. To solve this problem, we realize a coherent, flux-tunable, transmonlike qubit, which exhibits a frequency tunability range as small as 43 MHz, and whose frequency, anharmonicity and tunability range are set by a few experimentally achievable design parameters. Such a weakly tunable qubit may be used to avoid frequency collisions in a large lattice while exhibiting minimal susceptibility to flux noise.

DOI: [10.1103/PhysRevApplied.18.034057](https://doi.org/10.1103/PhysRevApplied.18.034057)

## I. INTRODUCTION

Quantum computers promise significant speedup, over their classical counterparts, for certain hard computational problems, such as factoring and quantum chemistry [1–3]. However, for quantum computers to achieve a clear advantage over classical computers they need to run error-correction codes and have sufficient quantum volumes [4]. One leading architecture for realizing such universal quantum computers is a crystal-like lattice of Josephson-junction-based qubits that supports the surface code or similar variations [5,6]. But to realize such a generic architecture, it is critical to employ high-coherence qubits that are simple to fabricate and characterize, and high-fidelity two-qubit gates that are fast, easy to tune up, and, preferably, require a minimal hardware overhead. Two leading candidates that have been shown to satisfy these requirements are single Josephson-junction (JJ) transmons [7–9] and cross-resonance gates, which are fully controlled by microwave signals [10,11]. In particular, single-JJ transmons, formed by capacitively shunting a JJ [see Fig. 1(a)], exhibit coherence times on the order of a few hundreds of microseconds [12], and cross-resonance gates, which realize CNOT gates by generating a ZX-like interaction

between two coupled qubits, regularly yield fidelities in excess of 99.1% with gate times of about 300 ns [13].

However, despite these favorable properties and numerous successful realizations of small quantum processors consisting of tens of single-JJ transmons and cross-resonance gates, deploying such qubits and gates in large quantum processors can be quite challenging. This is because cross-resonance gates, which are based on driving the control qubit at the target qubit frequency, set stringent lower and upper bounds on the first and second energy-level detunings of not only the control and target qubits but also their direct neighbors [14–18]. Satisfying these lower and upper bounds, which are necessary to avoid frequency collisions and slow gates, respectively, is particularly difficult to accomplish with single JJ transmons. The difficulty arises from the fact that their fixed frequencies  $f_q$  are primarily determined by the JJ energies, which owing to uncontrolled parameters in the fabrication process, have random scatter with a standard deviation  $\sigma_f$  that is comparable to the upper bounds of the required detunings (set by the qubit anharmonicity). Such imprecision in the occurring transmon frequencies significantly increases the likelihood of frequency collisions between neighboring qubits and decreases the yield of collision-free chips. For example, a “heavy hexagon” type lattice of qubits in a three-frequency pattern is shown to most effectively evade frequency collisions [14]. Yet even the smallest-sized such lattice, containing 23 qubits, if fabricated with conventional precision of  $\sigma_f/f_q \sim 3\%$ , will be collision-free only 0.1% of the time [14].

\*babdo@us.ibm.com

†Contributed equally to this work.

‡Current address: Center for Quantum Devices, Niels Bohr Institute, University of Copenhagen, 2100 Copenhagen, Denmark.

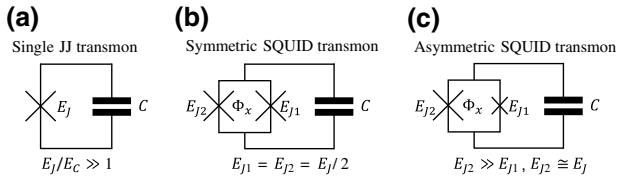


FIG. 1. Transmon circuits. (a) Fixed-frequency transmon consisting of a single Josephson junction with energy  $E_J$  shunted by a capacitor  $C$ . (b) Widely tunable transmon consisting of a symmetric dc SQUID with identical junctions  $E_{J1} = E_{J2} = E_J/2$  shunted by a capacitor  $C$ . The qubit frequency can be tuned using an external magnetic flux  $\Phi_x$  threading the SQUID loop. (c) Medium-range tunable transmon consisting of an asymmetric dc SQUID with dissimilar junctions  $E_{J2} \gg E_{J1}$ , where  $E_{J2} \cong E_J$ , shunted by a capacitor  $C$ .

To address this crippling frequency-collision problem in medium and large quantum processors, several strategies are being pursued, including (1) replacing the single JJ transmons with symmetric or asymmetric dc superconducting quantum interference device (SQUID) transmons [see Figs. 1(b) and 1(c)], whose frequency is tunable with external flux [7,19]; (2) combining single-JJ transmons with large-anharmonicity qubits, such as capacitively shunted flux qubits [20]; and (3) selectively modifying undesired transmon frequencies following fabrication and testing by etching a portion of their capacitive pads [21] or illuminating their JJs with focused laser beams for short durations [14,15]. The first strategy enables precise qubit frequency tuning and the second eases frequency crowding, but in either case the qubits will suffer dephasing when tuned away from their flux-insensitive “sweet spots.” The third strategy requires complex processing that is challenging to apply to large three-dimensional (3D) integrated and packaged processors. The best demonstrated precision of such schemes is  $\sigma_f = 14$  MHz, which can yield a collision-free 23-qubit device 70% of the time, but enables only 8% yield of a 127-qubit device and  $\ll 0.1\%$  yield at 1000 qubit scale [14].

Here, we realize a superconducting qubit, named weakly tunable qubit (WTQ), that retains the desirable properties of single-JJ transmons in multiqubit architectures and whose frequency tunes weakly with applied magnetic flux. Such a limited tunability could solve the frequency-collision problem in multiqubit architectures while maintaining high coherence. This tunability could also improve qubit relaxation times by evading two-level systems (TLSs) in frequency space. According to Ref. [22], shifting a qubit by about 10 MHz can decouple it from the TLS and restore the qubit’s  $T_1$ . Moreover, such a qubit could be beneficial in realizing high-fidelity parametric gates that rely on frequency modulation [23,24].

Prior to introducing the WTQ circuit, we briefly highlight the drawbacks of existing tunable transmons, namely,

the symmetric dc-SQUID transmon and the asymmetric dc-SQUID transmon, whose circuits are shown in Figs. 1(b) and 1(c). Since the frequency tunability range in the symmetric case can be large exceeding a gigahertz, its flux-noise sensitivity, which, to first order, increases with  $|df_q/d\Phi_x|$ , results in a significant dephasing away from the sweet spot [19]. In the asymmetric case on the other hand, a smaller tunability and sensitivity to flux noise can be achieved with large JJ-area ratio. Junction ratios of 15 to 1 are fabricated using conventional shadow evaporation, resulting in tunability of 330 MHz [19]. To reduce tunability to the minimum needed to avoid frequency collisions would require even larger ratios. However, since the Josephson energy of the large-size JJ in the asymmetric SQUID (i.e.,  $E_{J2}$ ) is comparable to that of the single-JJ transmon (i.e.,  $E_J$ ), a significantly thicker oxide is required in the fabrication process to yield  $E_{J2} \gg E_{J1}$  [see Fig. 1(c)]. Such a thick oxide requirement increases the probability of lossy two-level systems in the JJs, potentially limiting the qubit lifetime.

The outline of the remainder of the paper is as follows. In Sec. II, we introduce the WTQ circuit. In Sec. III, we derive the WTQ Hamiltonian. In Sec. IV, we present analytical formulas for the frequency and anharmonicity of the WTQ and calculated response of a WTQ example. In Sec. V, we calculate the relaxation and dephasing rates of WTQs. In Sec. VI, we present experimental results, i.e., spectroscopy and coherence, taken of two seven-qubit chips that incorporate six WTQs and a fixed-frequency transmon each. In Sec. VII, we discuss the measurement results, offer additional theoretical predictions, and outline possible enhancements and future directions. Finally, in Sec. VIII, we provide a brief summary and highlight the advantages of employing WTQs in large quantum processors.

## II. THE WTQ CIRCUIT

The WTQ circuit consists of three Josephson junctions  $J_1, J_2, J_3$  with self-capacitances  $C_{J1}, C_{J2}, C_{J3}$ , respectively, and three capacitors  $C_1, C_2$ , and  $C_c$  as shown in Fig. 2. The junctions  $J_2$  and  $J_3$  form a SQUID loop, which is connected in series with the junction  $J_1$ . The junction  $J_1$  shunted by the capacitance  $C_1$  provides the main transmon mode of the qubit. The SQUID shunted by the capacitance  $C_2$  generates a second transmon-type mode whose frequency is tuned by the external flux bias  $\Phi_x$  threading the SQUID loop. Asymmetry is introduced in the SQUID by making the areas of the junctions  $J_2$  and  $J_3$  unequal to reduce the sensitivity to the flux noise [19]. The tunability of the qubit mode is achieved by the electrostatic interaction of the junction  $J_1$  with the SQUID through the capacitance  $C_c$ .

In general, the underlying physics of WTQs is very similar to that of tunable coupling qubits (TCQs) [25–28],

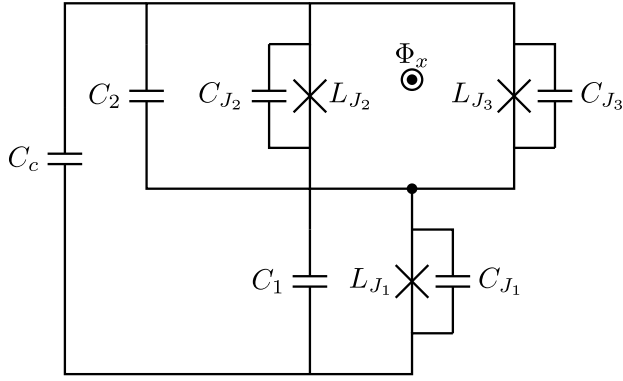


FIG. 2. Circuit diagram of the WTQ. It consists of three Josephson junctions with inductances  $L_{J_1}$ ,  $L_{J_2}$ ,  $L_{J_3}$  and self-capacitances  $C_{J_1}$ ,  $C_{J_2}$ ,  $C_{J_3}$ , respectively. The critical currents of the junctions are related to their inductances by the relation  $I_{c,i} = \Phi_0/2\pi L_{J_i}$ , for  $i = 1, 2, 3$ . The SQUID loop formed by the junctions  $J_2$  and  $J_3$  is biased by the external dc flux  $\Phi_x$ . The sensitivity of the SQUID loop to the flux noise is reduced by making the areas of the junctions  $J_2$  and  $J_3$  unequal, i.e.,  $I_{c,3} = \rho_J I_{c,2}$  for some  $\rho_J > 1$ . Capacitors  $C_1$  and  $C_2$  shunting the junctions create the two main modes of the circuit: the qubit mode formed by  $J_1$  shunted with  $C_1$  and the high-frequency mode formed by  $C_2$  shunting the SQUID loop. The electrostatic interaction of the qubit mode with the SQUID through the capacitance  $C_c$  provides the tunability of the WTQ.

which also consist of two capacitively coupled transmons. TCQs and WTQs, however, differ in their circuit and functionality. While TCQs employ nominally identical symmetric SQUID transmons, WTQs employ single-JJ and asymmetric SQUID transmons. TCQs also allow independent tuning of their frequency and coupling strength to the readout resonator, whereas WTQs mainly enable their frequency to be tuned within a small range.

### III. DERIVATION OF THE WTQ HAMILTONIAN

We apply the circuit quantization formalism developed in Ref. [29] to derive the Hamiltonian of the WTQ circuit and employ the analysis technique described in Ref. [30] to make a Born-Oppenheimer approximation and calculate the decoherence rates. To better describe the coupling of the WTQ to the flux bias circuitry we introduce a more detailed circuit model of the flux bias mechanism as shown in Fig. 3. The flux bias in the SQUID loop is generated by the dc current source  $I_B$  with impedance  $Z(\omega)$ . Note that this construction is quite general in the sense that a wide range of circuits can be represented with this simple model by Norton's theorem. The flux is coupled to the SQUID loop by a coil of inductance  $L_c$ . We introduce two partial inductances  $L_1$  and  $L_2$  [31] to model the linear inductance of the SQUID loop, which are coupled to the bias coil with mutual inductances  $M_1$  and  $M_2$ . The finely detailed circuit model in Fig. 3 that carefully models the

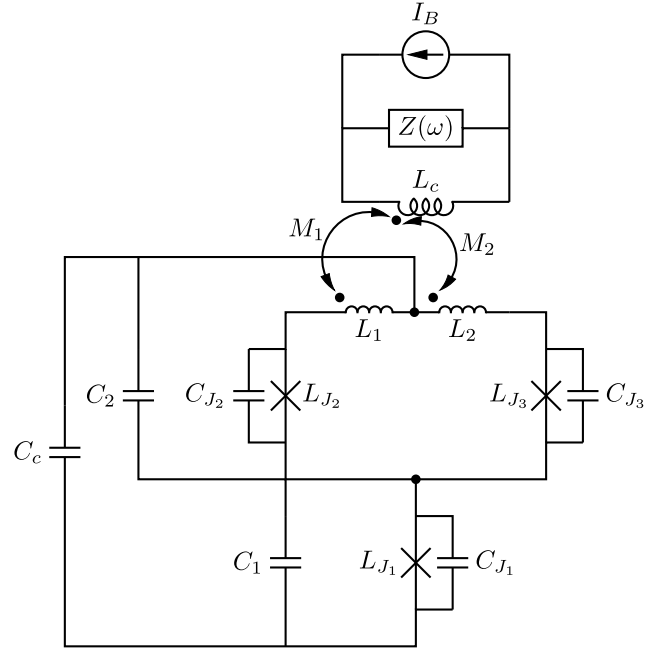


FIG. 3. Detailed WTQ circuit diagram. The flux bias in the SQUID loop is generated by the dc current source  $I_B$  with impedance  $Z(\omega)$ .  $L_c$  is the inductance of the coil that produces the magnetic field threading the SQUID loop. Two partial inductances [31]  $L_1$  and  $L_2$  are introduced to model the linear inductance of the SQUID loop, which are inductively coupled to the coil with mutual inductances  $M_1$  and  $M_2$ , respectively. Such a finely detailed construction of the WTQ circuit avoids inconsistencies in the calculation of the decoherence rates.

inductive network of the WTQ circuit and the flux bias circuitry is crucial for avoiding ambiguities in the calculation of the decoherence rates [32,33]. Our Born-Oppenheimer treatment of the inductive network of the WTQ circuit, which reduces the capacitance matrix to unity, finds the irrotational gauge discussed in Ref. [32] that removes the inconsistencies associated with a gauge freedom.

Before applying the formalism in Ref. [29] we transform the capacitive network in the original WTQ circuit in Fig. 3 with the help of the multiport Belevitch transformer  $\mathbf{T}$  as shown in Fig. 4. This transformation reduces the number of capacitors by one and helps us bring the circuit to a form treatable in the formalism of Ref. [29] by making the capacitance matrix of the circuit diagonal:

$$\mathbf{C}_0 = \begin{pmatrix} C_A & 0 & 0 & 0 \\ 0 & C_{J_2} & 0 & 0 \\ 0 & 0 & C_{J_3} & 0 \\ 0 & 0 & 0 & C_B \end{pmatrix}, \quad (1)$$

where  $C_A = C_1 + C_{J_1} + C_c C_2 / C_2 + C_c$  and  $C_B = C_2 + C_c$ .

Also, since the number of degrees of freedom is given by the number of capacitors in the minimum spanning tree of the circuit, we reduce the number of degrees of freedom

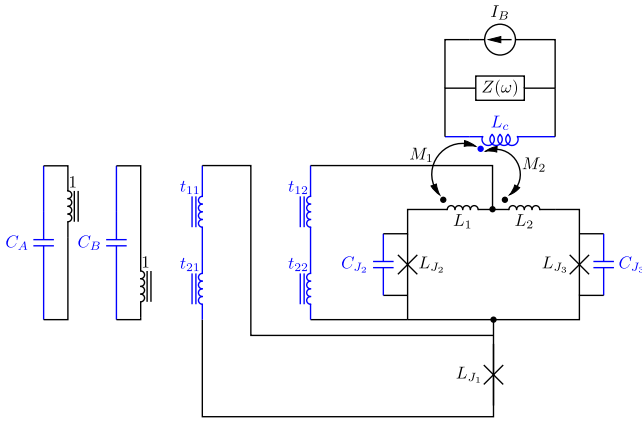


FIG. 4. Multiport Belevitch transformer with a turns-ratio matrix  $\mathbf{T}$  is introduced to reduce the number of capacitors by one. The capacitance values are  $C_A = C_1 + C_{J_1} + C_c C_2 / C_2 + C_c$  and  $C_B = C_2 + C_c$ . The turns-ratios are  $t_{11} = 1$ ,  $t_{12} = C_c / C_2 + C_c$ ,  $t_{21} = 0$ , and  $t_{22} = 1$ . Note that  $C_{J_1}$  is added with  $C_1$  and contributes to the value of the capacitance  $C_A$ . In blue are the branches corresponding to the spanning tree. The remaining branches are the chord branches that define the fundamental loop matrix in Eq. (3) [29]. The multiport Belevitch transformer is eliminated according to Ref. [34] to arrive at the effective fundamental loop matrix in Eq. (3).

by one. The Belevitch transformer turns-ratio matrix  $\mathbf{T}$  is given by

$$\mathbf{T} = \begin{pmatrix} t_{11} & t_{12} \\ t_{21} & t_{22} \end{pmatrix} = \begin{pmatrix} 1 & \frac{C_c}{C_2 + C_c} \\ 0 & 1 \end{pmatrix}, \quad (2)$$

which is obtained by a Cholesky decomposition of the  $2 \times 2$  impedance matrix defined looking into the purely capacitive network consisting of the capacitances  $C_1$ ,  $C_2$ , and  $C_c$ .

The fundamental loop matrix defined in Ref. [29] is given by

$$\mathbf{F}_{CL} = \begin{pmatrix} -t_{12} & t_{12} \\ 1 & 0 \\ 0 & -1 \\ -t_{22} & t_{22} \end{pmatrix} = \begin{pmatrix} -\frac{C_c}{C_2 + C_c} & \frac{C_c}{C_2 + C_c} \\ 1 & 0 \\ 0 & -1 \\ -1 & 1 \end{pmatrix}. \quad (3)$$

Note that the fundamental loop matrix of Ref. [29] is generalized to have real entries (turns ratios) other than 0, 1, and  $-1$  [34].

The branches of the spanning tree are indicated in blue in Fig. 4. The remaining branches are chord branches that define the fundamental loop matrix. The effective loop matrix in Eq. (3) is obtained by eliminating the multiport Belevitch transformer defined in Eq. (2) using the technique introduced in Ref. [34].

We use Eq. (62) of Ref. [29] to calculate the inverse inductance matrix  $\mathbf{M}_0$  as

$$\mathbf{M}_0 = \mathbf{F}_{CL} \tilde{\mathbf{L}}_L^{-1} \tilde{\mathbf{L}}_L^{-1} \mathbf{F}_{CL}^T. \quad (4)$$

To be able to calculate  $\mathbf{M}_0$  we need to first introduce some auxiliary matrices related to the inductive network in the circuit that are defined in Ref. [29]. The inductance matrix  $\mathbf{L}_t$  is defined in Eq. (1) of Ref. [29] as

$$\mathbf{L}_t = \begin{pmatrix} \mathbf{L} & \mathbf{L}_{LK} \\ \mathbf{L}_{LK}^T & \mathbf{L}_K \end{pmatrix} \quad (5)$$

$$= \begin{pmatrix} L_1 & 0 & M_1 \\ 0 & L_2 & M_2 \\ M_1 & M_2 & L_c \end{pmatrix}. \quad (6)$$

The inductance matrix  $\mathbf{L}_t$  defined above is partitioned according to the choice of the tree and chord inductors in the network and the subscripts  $L$  and  $K$  denote chord and tree inductors, respectively. Hence  $L_1$  and  $L_2$  are chord inductors, whereas  $L_c$  is a tree inductor.

In general, there will be a nonzero mutual inductance  $M_{12}$  between  $L_1$  and  $L_2$ . However, such a mutual inductance will only bring corrections of order  $(M_{12}/L_1)$  and  $(M_{12}/L_2)$ , which are small because  $L_1$  and  $L_2$  are much larger than  $M_{12}$ . Therefore, we assume above  $M_{12} = 0$  to avoid complicating the analytical treatment.

Equations (32) and (33) of Ref. [29] define the matrices  $\tilde{\mathbf{L}}$  and  $\tilde{\mathbf{L}}_K$  as

$$\tilde{\mathbf{L}} = \mathbf{L} - \mathbf{L}_{LK} \mathbf{L}_K^{-1} \mathbf{L}_{LK}^T \quad (7)$$

$$= \begin{pmatrix} L_1 - \frac{M_1^2}{L_c} & -\frac{M_1 M_2}{L_c} \\ -\frac{M_1 M_2}{L_c} & L_2 - \frac{M_2^2}{L_c} \end{pmatrix}, \quad (8)$$

$$\tilde{\mathbf{L}}_K = \mathbf{L}_K - \mathbf{L}_{LK}^T \mathbf{L}^{-1} \mathbf{L}_{LK} \quad (9)$$

$$= L_c (1 - k_1^2 - k_2^2), \quad (10)$$

where we define the inductive coupling coefficients  $k_1$  and  $k_2$  as  $k_1 = M_1 / \sqrt{L_c L_1}$  and  $k_2 = M_2 / \sqrt{L_c L_2}$ .  $\tilde{\mathbf{L}}_K$  turns out to be a scalar since we have only  $L_c$  as a tree inductor in our circuit.

Next, we borrow some more definitions from Ref. [29] that are used in the definition of  $\mathbf{M}_0$  in Eq. (4) above. Equation (42) of Ref. [29] reads

$$\tilde{\mathbf{F}}_{KL} = \mathbf{F}_{KL} - \mathbf{L}_K^{-1} \mathbf{L}_{LK}^T \quad (11)$$

$$= -\frac{1}{L_c} \begin{pmatrix} M_1 & M_2 \end{pmatrix}, \quad (12)$$

where we use the fact that  $\mathbf{F}_{KL} = \begin{pmatrix} 0 & 0 \end{pmatrix}$  since the only tree inductor  $L_c$  does not belong to any of the fundamental loops defined by the chord inductors  $L_1$  and  $L_2$ . Equation

(41) of Ref. [29] defines another auxiliary inductance matrix  $\tilde{\mathbf{L}}_K$  as

$$\tilde{\mathbf{L}}_K = (\mathbf{1}_K - \mathbf{L}_K \tilde{\mathbf{F}}_{KL} \mathbf{L}^{-1} \mathbf{L}_{LK} \tilde{\mathbf{L}}_K^{-1})^{-1} \mathbf{L}_K \quad (13)$$

$$= L_c (1 - k_1^2 - k_2^2). \quad (14)$$

Again, similar to  $\tilde{\mathbf{L}}_K$  calculated above  $\tilde{\mathbf{L}}_K$  turns out to be a scalar since we have only  $L_c$  as a tree inductor in the circuit. Next, we calculate two more matrices that appear in the definition of  $\mathbf{M}_0$  in Eq. (4) above. Equation (51) of Ref. [29] defines the matrix  $\mathbf{L}_{LL}$  as

$$\mathbf{L}_{LL} = \tilde{\mathbf{L}} + \mathbf{F}_{KL}^T \tilde{\mathbf{L}}_K \tilde{\mathbf{F}}_{KL} \quad (15)$$

$$= \tilde{\mathbf{L}}, \quad (16)$$

since  $\mathbf{F}_{KL} = (0 \ 0)$  as we note above. Equation (47) of Ref. [29] defines the matrix  $\tilde{\mathbf{L}}_L$  as

$$\tilde{\mathbf{L}}_L^{-1} = (\mathbf{1}_L + \mathbf{L}^{-1} \mathbf{L}_{LK} \tilde{\mathbf{L}}_K^{-1} \tilde{\mathbf{L}}_K \tilde{\mathbf{F}}_{KL}) \tilde{\mathbf{L}}^{-1} \quad (17)$$

$$= \begin{pmatrix} 1/L_1 & 0 \\ 0 & 1/L_2 \end{pmatrix}. \quad (18)$$

Using the definitions above we can now evaluate the expression for  $\mathbf{M}_0$  given in Eq. (4) as

$$\mathbf{M}_0 = \mathbf{F}_{CL} \begin{pmatrix} 1/L_1 & 0 \\ 0 & 1/L_2 \end{pmatrix} \mathbf{F}_{CL}^T \quad (19)$$

$$= \begin{pmatrix} t_{12}^2 \left( \frac{1}{L_1} + \frac{1}{L_2} \right) & -\frac{t_{12}}{L_1} & -\frac{t_{12}}{L_2} & t_{12} \left( \frac{1}{L_1} + \frac{1}{L_2} \right) \\ -\frac{t_{12}}{L_1} & \frac{1}{L_1} & 0 & -\frac{1}{L_1} \\ -\frac{t_{12}}{L_2} & 0 & \frac{1}{L_2} & -\frac{1}{L_2} \\ t_{12} \left( \frac{1}{L_1} + \frac{1}{L_2} \right) & -\frac{1}{L_1} & -\frac{1}{L_2} & \frac{1}{L_1} + \frac{1}{L_2} \end{pmatrix}. \quad (20)$$

The coupling vector  $\mathbf{S}_0$  to the current source  $I_B$  is calculated using Eq. (66) of Ref. [29] as

$$\mathbf{S}_0 = \mathbf{F}_{CB} - \mathbf{F}_{CL} (\mathbf{L}_{LL}^{-1})^T \tilde{\mathbf{F}}_{KL}^T \tilde{\mathbf{L}}_K^T \mathbf{F}_{KB} \quad (21)$$

$$= \begin{pmatrix} t_{12} \left( (1 - k_2^2) \frac{M_1}{L_1} - (1 - k_1^2) \frac{M_2}{L_2} + k_1 k_2 \frac{(M_2 - M_1)}{\sqrt{L_1 L_2}} \right) \\ -(1 - k_2^2) \frac{M_1}{L_1} - k_1 k_2 \frac{M_2}{\sqrt{L_1 L_2}} \\ (1 - k_1^2) \frac{M_2}{L_2} + k_1 k_2 \frac{M_1}{\sqrt{L_1 L_2}} \\ (1 - k_2^2) \frac{M_1}{L_1} - (1 - k_1^2) \frac{M_2}{L_2} + k_1 k_2 \frac{(M_2 - M_1)}{\sqrt{L_1 L_2}} \end{pmatrix} \quad (22)$$

$$\cong \begin{pmatrix} t_{12} \left( \frac{M_1}{L_1} - \frac{M_2}{L_2} \right) \\ -\frac{M_1}{L_1} \\ \frac{M_2}{L_2} \\ \frac{M_1}{L_1} - \frac{M_2}{L_2} \end{pmatrix}, \quad (23)$$

using the auxiliary matrices introduced above and noting that  $\mathbf{F}_{CB} = 0$  since none of the capacitors in the WTQ circuit belongs to the fundamental loop defined by the chord branch corresponding to the dc current source  $I_B$  and  $\mathbf{F}_{KB} = -1$ . In the last line above we use the fact that the inductive coupling constants  $k_1, k_2$  are small; in other words,  $k_1, k_2 \ll 1$  to simplify the expressions. We note here that the coupling vector  $\tilde{\mathbf{m}}_0$  [defined in Eq. (65) of Ref. [29]] to the impedance  $Z(\omega)$  is given by

$$\tilde{\mathbf{m}}_0 = \mathbf{F}_{CZ} - \mathbf{F}_{CL} (\mathbf{L}_{LL}^{-1})^T \tilde{\mathbf{F}}_{KL}^T \tilde{\mathbf{L}}_K^T \mathbf{F}_{KZ} \quad (24)$$

$$= -\mathbf{S}_0, \quad (25)$$

since  $\mathbf{F}_{CZ} = 0$  and  $\mathbf{F}_{KZ} = 1$ . We use  $\tilde{\mathbf{m}}_0$  in later sections to calculate the decoherence rates of the WTQ.

Hence, we can write the Hamiltonian of the WTQ circuit in the initial frame as

$$\mathcal{H} = \frac{1}{2} \mathbf{Q}^T \mathbf{C}_0^{-1} \mathbf{Q} + \frac{1}{2} \Phi^T \mathbf{M}_0 \Phi + \Phi^T \mathbf{S}_0 I_B - \sum_{i=1}^3 E_{J_i} \cos(\varphi_{J_i}), \quad (26)$$

where  $\Phi = \Phi_0/2\pi (\varphi_{J_1}, \varphi_{J_2}, \varphi_{J_3}, \varphi_4)$ . Here, the first three coordinates are the phases across the junctions whereas the last coordinate  $\varphi_4$  is the phase across the capacitor  $C_B$ .  $\mathbf{Q}$  is the vector of charge variables canonically conjugate to the fluxes  $\Phi$ .

To find the dc flux bias developed across each junction in the limit of small loop inductances  $L_1 \rightarrow 0, L_2 \rightarrow 0$  and to determine the coupling of the WTQ to the impedance  $Z(\omega)$  we need to perform a few coordinate transformations:

$$\mathbf{R}_0 = \begin{pmatrix} 1 & 0 & 0 & 0 \\ t_{12} & 1 & 0 & 1 \\ t_{12} & 0 & 1 & 1 \\ 0 & 0 & 0 & 1 \end{pmatrix}, \quad (27)$$

$$\mathbf{R}_1 = \begin{pmatrix} 1 & 0 & 0 & 0 \\ 0 & 1 & 0 & 0 \\ 0 & 0 & 1 & 0 \\ -t_{12} \frac{(C_{J_2} + C_{J_3})}{C_b} & -\frac{C_{J_2}}{C_b} & -\frac{C_{J_3}}{C_b} & 1 \end{pmatrix}, \quad (28)$$

$$\mathbf{R}_2 = \begin{pmatrix} 1 & -\frac{C_{J_2} C_c}{C_a C_b} & -\frac{C_{J_3} C_c}{C_a C_b} & 0 \\ 0 & 1 & 0 & 0 \\ 0 & 0 & 1 & 0 \\ 0 & 0 & 0 & 1 \end{pmatrix}, \quad (29)$$

where we define

$$C_a = C_1 + \frac{C_2 C_c}{C_2 + C_c}, \quad (30)$$

$$C_b = C_2 + C_c + C_{J_2} + C_{J_3}, \quad (31)$$

with  $C'_1 = C_1 + C_{J_1}$  and  $C'_2 = C_2 + C_{J_2} + C_{J_3}$ . Next we do a capacitance rescaling as required by the Born-Oppenheimer treatment of Ref. [30]

$$\mathbf{A} = \begin{pmatrix} \sqrt{C_a} & 0 & 0 & 0 \\ 0 & \sqrt{C_{11}} & -\beta\sqrt{C_{22}} & 0 \\ 0 & 0 & \sqrt{C_{22}} & 0 \\ 0 & 0 & 0 & \sqrt{C_b} \end{pmatrix}, \quad (32)$$

with

$$C_{11} = C_{J_2} \frac{C_{\alpha,3} C_{\beta,3}}{C_a C_b}, \quad (33)$$

$$C_{22} = C_{J_3} \frac{C_A C_B}{C_{\alpha,3} C_{\beta,3}}, \quad (34)$$

$$\beta = \sqrt{\frac{C_{J_2} C_{J_3}}{C_a C_b} \frac{(C'_1 + C_c)}{\sqrt{C_A C_B}}}, \quad (35)$$

and

$$C_{\alpha,3} = C'_1 + \frac{C_c (C_2 + C_{J_3})}{C_2 + C_c + C_{J_3}}, \quad (36)$$

$$C_{\beta,3} = C_2 + C_c + C_{J_3}. \quad (37)$$

All four coordinate transformations can be combined into one, i.e.,  $\mathbf{R}_t$ , such that

$$\mathbf{R}_t = \mathbf{R}_0 \mathbf{R}_1 \mathbf{R}_2 \mathbf{A}^{-1}. \quad (38)$$

The initial capacitance matrix  $\mathbf{C}_0$  is transformed into the identity matrix by the total transformation  $\mathbf{R}_t$  as

$$\mathbf{C}_0 \rightarrow \mathbf{R}_t^T \mathbf{C}_0 \mathbf{R}_t = \mathbf{1}. \quad (39)$$

This ensures the choice of the irrotational gauge that removes the inconsistencies in the decoherence rate calculations as discussed in Ref. [32].

Initial flux coordinate vector  $\Phi$  is transformed into the final capacitance rescaled coordinate vector  $\mathbf{f}$  by

$$\Phi = \mathbf{R}_t \mathbf{f}. \quad (40)$$

Phases across the junctions can be written in terms of the final coordinates  $\mathbf{f} = (f_1, f_2, f_3, f_4)^T$  as

$$\varphi_{J_1} = \alpha_{11} f_1 + \alpha_{12} f_2 + \alpha_{13} f_3 + \alpha_{14} f_4, \quad (41)$$

$$\varphi_{J_2} = \alpha_{21} f_1 + \alpha_{22} f_2 + \alpha_{23} f_3 + \alpha_{24} f_4, \quad (42)$$

$$\varphi_{J_3} = \alpha_{31} f_1 + \alpha_{32} f_2 + \alpha_{33} f_3 + \alpha_{34} f_4, \quad (43)$$

with

$$\alpha_{11} = \frac{1}{\sqrt{C_a}}, \quad \alpha_{21} = \left(\frac{C_c}{C_b}\right) \frac{1}{\sqrt{C_a}}, \quad \alpha_{31} = \left(\frac{C_c}{C_b}\right) \frac{1}{\sqrt{C_a}}, \quad (44)$$

$$\alpha_{14} = 0, \quad \alpha_{24} = \frac{1}{\sqrt{C_b}}, \quad \alpha_{34} = \frac{1}{\sqrt{C_b}}, \quad (45)$$

$$\alpha_{12} = -\frac{C_c \sqrt{C_{J_2}}}{\sqrt{C_a C_b C_{\alpha,3} C_{\beta,3}}}, \quad \alpha_{13} = -\frac{C_c \sqrt{C_{J_3}}}{\sqrt{C_A C_B C_{\alpha,3} C_{\beta,3}}}, \quad (46)$$

$$\alpha_{22} = \frac{1}{\sqrt{C_{J_2}}} \sqrt{\frac{C_{\alpha,3} C_{\beta,3}}{C_a C_b}}, \quad \alpha_{23} = 0, \quad (47)$$

$$\alpha_{32} = -\frac{(C'_1 + C_c) \sqrt{C_{J_2}}}{\sqrt{C_a C_b C_{\alpha,3} C_{\beta,3}}}, \quad \alpha_{33} = \frac{1}{\sqrt{C_{J_3}}} \sqrt{\frac{C_A C_B}{C_{\alpha,3} C_{\beta,3}}}. \quad (48)$$

Hence, we can write the system Hamiltonian in the capacitance rescaled final coordinates  $\mathbf{f}$  as

$$\mathcal{H} = \frac{1}{2} \mathbf{q}_f^T \mathbf{q}_f + U(\mathbf{f}), \quad (49)$$

where  $\mathbf{q}_f$  is the vector of momenta canonically conjugate to the final coordinates  $\mathbf{f}$  and the potential  $U(\mathbf{f})$  is given by

$$U(\mathbf{f}) = \frac{1}{2} \mathbf{f}^T \mathbf{R}_t^T \mathbf{M}_0 \mathbf{R}_t \mathbf{f} + \mathbf{f}^T \mathbf{R}_t^T \mathbf{S}_0 I_B - \sum_{i=1}^3 E_{J_i} \cos(\varphi_{J_i}). \quad (50)$$

### A. Born-Oppenheimer approximation

We perform the Born-Oppenheimer approximation following Ref. [30]. The coordinates  $f_2$  and  $f_3$  are fast coordinates denoted by the vector  $\mathbf{f}_\perp = (f_2, f_3)$  and will be eliminated. Since the potential seen is very steep along the direction of the fast coordinates it can be approximated with a harmonic potential as given by the Eq. (14) in Ref. [30]

$$U(\mathbf{f}) \approx V(\mathbf{f}_\parallel) + \sum_i a_i(\mathbf{f}_\perp)_i + \sum_{ij} b_{ij}(\mathbf{f}_\perp)_i (\mathbf{f}_\perp)_j, \quad (51)$$

where  $\mathbf{f}_\parallel = (f_1, f_4)$  is the vector holding the slow coordinates and the matrix  $\mathbf{b} = [b_{ij}]$  is the  $2 \times 2$  sector (corresponding to the coordinates  $f_2$  and  $f_3$ ) of the transformed  $\mathbf{M}_0$  matrix in the final frame; in other words, of the matrix

$\mathbf{R}_l^T \mathbf{M}_0 \mathbf{R}_l$ :

$$\mathbf{b} = \begin{pmatrix} \frac{1}{\alpha_{22}^2 C_{J_2}^2 L_1} & \frac{1}{C_{23} L_1} \\ \frac{1}{C_{23} L_1} & \frac{1}{\alpha_{33}^2 C_{J_3}^2 L_2} + \frac{(C_1 + C_c)^2 C_{J_3}}{C_A C_B C_{\alpha,3} C_{\beta,3} L_1} \end{pmatrix}, \quad (52)$$

where we define  $C_{23}^{-1} = \sqrt{C_{J_3} C_a C_b / C_{J_2} C_A C_B (C_1 + C_c) / C_{\alpha,3} C_{\beta,3} L_1}$ . The vector  $\mathbf{a} = (a_1, a_2)$  in Eq. (51) holds the entries (corresponding to the fast coordinates  $f_2$  and  $f_3$ ) of the transformed  $\mathbf{S}_0$  vector in the final frame; in other words, of the vector  $\mathbf{R}_l^T \mathbf{S}_0$  (with the scale factor  $I_B / \varphi_0$ ):

$$\mathbf{a} = \begin{pmatrix} -\frac{M_1}{\alpha_{22} C_{J_2} L_1} \\ -\frac{(C_1 + C_c) \sqrt{C_{J_3} M_1}}{\sqrt{C_A C_B C_{\alpha,3} C_{\beta,3} L_1}} + \frac{M_2}{\alpha_{33} C_{J_3} L_2} \end{pmatrix} \begin{pmatrix} I_B \\ \varphi_0 \end{pmatrix}, \quad (53)$$

where  $\varphi_0 \equiv \Phi_0 / 2\pi$  is the reduced flux quantum.

One can verify that  $f_2$  and  $f_3$  are indeed fast degrees of freedom by checking the diagonal entries in Eq. (52), which give squared frequencies in units of (rad/sec)<sup>2</sup>. Using Eqs. (47) and (48) these frequencies can be seen to be very nearly equal to  $1/(C_{J_2} L_1)$  and  $1/(C_{J_3} L_2)$ , which are much larger than the frequencies of the qubit and SQUID modes that are mainly determined by the junction inductances  $L_{J_1}$ ,  $L_{J_2}$ , and  $L_{J_3}$  and the geometric capacitances  $C_1$ ,  $C_2$ ,  $C_c$  that are much larger compared to  $L_1$  and  $L_2$  and  $C_{J_2}$  and  $C_{J_3}$ , respectively.

The potential is centered around

$$(\mathbf{f}_{\perp}^{\min})_0 = \begin{pmatrix} \alpha_{22} C_{J_2} \left( M_1 + \frac{(C_1 + C_c) C_{J_3}}{C_{\alpha,3} C_{\beta,3}} M_2 \right) \\ -\alpha_{33} C_{J_3} M_2 \end{pmatrix} \begin{pmatrix} I_B \\ \varphi_0 \end{pmatrix} \quad (54)$$

for the fast coordinates (here, we drop terms quadratic in the small inductive coupling coefficients  $k_1, k_2$ ). This is the dc component of the fast coordinates that does not depend on the slow coordinates. We use Eq. (16) of Ref. [30] to calculate  $(\mathbf{f}_{\perp}^{\min})_0$ :

$$(\mathbf{f}_{\perp}^{\min})_0 = -\frac{1}{2} \mathbf{b}^{-1} \mathbf{a}. \quad (55)$$

Hence, the reduced dc flux bias in the phases of the junctions is

$$\boldsymbol{\varphi}_x^{(0)} = \begin{pmatrix} \varphi_{x,1}^{(0)} \\ \varphi_{x,2}^{(0)} \\ \varphi_{x,3}^{(0)} \end{pmatrix} = \begin{pmatrix} \alpha_{12} & \alpha_{13} \\ \alpha_{22} & \alpha_{23} \\ \alpha_{32} & \alpha_{33} \end{pmatrix} (\mathbf{f}_{\perp}^{\min})_0 \quad (56)$$

$$= \begin{pmatrix} \frac{C_c (C_{J_3} M_2 - C_{J_2} M_1)}{C_a C_b} \\ \frac{C_{\alpha,3} C_{\beta,3}}{C_a C_b} M_1 + \frac{(C_1 + C_c) C_{J_3}}{C_a C_b} M_2 \\ -\frac{(C_1 + C_c) C_{J_2}}{C_a C_b} M_1 - \frac{C_{\alpha,2} C_{\beta,2}}{C_a C_b} M_2 \end{pmatrix} \begin{pmatrix} I_B \\ \varphi_0 \end{pmatrix}, \quad (57)$$

where we define

$$C_{\alpha,2} = C_1 + \frac{C_c (C_2 + C_{J_2})}{C_2 + C_c + C_{J_2}}, \quad (58)$$

$$C_{\beta,2} = C_2 + C_c + C_{J_2}. \quad (59)$$

We note here that  $\varphi_x = \varphi_{x,2}^{(0)} - \varphi_{x,3}^{(0)} = (M_1 + M_2) (I_B / \varphi_0)$ , as expected.

We perform the Born-Oppenheimer approximation by expanding the cosine potentials around the dc flux biases in Eq. (54) for the fast coordinates to obtain the following effective Hamiltonian:

$$\mathcal{H} = \frac{1}{2} \mathbf{q}^T \mathcal{C}^{-1} \mathbf{q} - E_{J_1} \cos(\varphi_1 + \varphi_{x,1}^{(0)}) - E_2 \cos(\varphi_2 + \varphi_x^{(2)}), \quad (60)$$

where

$$\mathcal{C} = \begin{pmatrix} C_1 + C_c & -C_c \\ -C_c & C_2 + C_c \end{pmatrix}, \quad (61)$$

$$E_2 = (E_{J_2} + E_{J_3}) \cos\left(\frac{\varphi_x}{2}\right) \sqrt{1 + d^2 \tan^2\left(\frac{\varphi_x}{2}\right)}, \quad (62)$$

$$\varphi_x^{(2)} = \frac{(\varphi_{x,2}^{(0)} + \varphi_{x,3}^{(0)})}{2} - \tan^{-1}\left(d \tan\left(\frac{\varphi_x}{2}\right)\right), \quad (63)$$

with  $d = (E_{J_3} - E_{J_2}) / (E_{J_2} + E_{J_3})$ ,  $\varphi_1 = f_1 / \sqrt{C_a}$ ,  $\varphi_2 = f_2 / \sqrt{C_b}$ ,  $E_{J_1} = \varphi_0 I_{J_1}$ ,  $E_{J_2} = \varphi_0 I_{J_2}$ , and  $E_{J_3} = \varphi_0 I_{J_3}$ .

Equation (60) is the Hamiltonian corresponding to two transmon qubits with Josephson energies  $E_{J_1}$  and  $E_2$  and shunting capacitances  $C_1$  and  $C_2$  coupled electrostatically with capacitance  $C_c$ . In other words, the WTQ mode associated with the shunt capacitance  $C_1$  and Josephson energy  $E_{J_1}$  determines the bare qubit mode, whereas the mode associated with the shunt capacitance  $C_2$  and effective Josephson energy  $E_2$  determines the bare SQUID mode. In the next section, we calculate the dressed frequencies with a perturbative treatment of the Hamiltonian in Eq. (60).

#### IV. WTQ FREQUENCY AND ANHARMONICITY

At this point we can calculate the qubit frequency  $\omega_q$  using formulas derived in Ref. [35]

$$\omega_q = \omega_1 \sqrt{1 - \frac{r^2 \omega_1^2}{\omega_2^2 - (1 - r^2) \omega_1^2}}, \quad (64)$$

where  $\omega_1$  is the bare frequency of the qubit mode given by [35]

$$\omega_1 = \omega_{J_1} - \frac{E_{C_1} / \hbar}{1 - E_{C_1} / (\hbar \omega_{J_1})}, \quad (65)$$

with

$$E_{C_1} = \frac{e^2}{2(C'_1 + C_c)}, \quad (66)$$

and

$$\omega_{J_1} = \frac{1}{\sqrt{L_{J_1}(C'_1 + C_c)}}. \quad (67)$$

The coupling coefficient  $r$  in Eq. (64) between the modes of the WTQ is defined by

$$r = \frac{C_c}{\sqrt{C'_1 C'_2 + C_c(C'_1 + C'_2)}}. \quad (68)$$

The charging energy  $E_{C_2}$  for the high-frequency SQUID mode is

$$E_{C_2} = \frac{e^2(1+r^2)}{2(C'_2 + C_c)}. \quad (69)$$

Bare frequency  $\omega_2$  of the SQUID mode is given by

$$\omega_2 = \omega_{J_2} - \frac{E_{C_2}/\hbar}{1 - E_{C_2}/(\hbar\omega_{J_2})}, \quad (70)$$

with

$$\omega_{J_2} = \frac{1}{\sqrt{L_{J_S} \frac{(C'_2 + C_c)}{(1+r^2)}}}, \quad (71)$$

where we define the effective SQUID inductance  $L_{J_S}$

$$L_{J_S} = \left( \left( \frac{1}{L_{J_2}} + \frac{1}{L_{J_3}} \right) \left| \cos\left(\frac{\varphi_x}{2}\right) \right| \sqrt{1 + d^2 \tan^2\left(\frac{\varphi_x}{2}\right)} \right)^{-1}. \quad (72)$$

Anharmonicity  $\alpha$  of the qubit mode can be estimated by [35]

$$\alpha = -E_{C_1} \left( \frac{\omega_{J_1}}{\omega_1} \right)^2 \left( 1 - \frac{r^2 \omega_1^2}{\omega_2^2 - (1-r^2)\omega_1^2} \right)^3. \quad (73)$$

In Figs. 5(a) and 5(b) we plot the transition frequency  $f_{01} = f_q = \omega_q/2\pi$  and the anharmonicity  $\alpha$  of a WTQ as a function of the normalized applied flux. The device parameters in this example are chosen to yield a WTQ with  $f_{01}^{\max}$  and  $\alpha$  of about 5 GHz and 300 MHz, respectively, and frequency tunability  $\delta = 50$  MHz. In the calculation, we use the analytical formulas of Eqs. (64) and (73), which we plot as red dashed curves and compare them to the

results obtained using the exact diagonalization of the qubit Hamiltonian specified in Eq. (60) in the charge basis (Bloch-wave basis), which we plot as blue solid curves. As seen in Fig. 5(b), the WTQ anharmonicity varies with the applied flux. But the variation is relatively small of about 17 MHz in this example, between the minimum and maximum sweet spots (based on the exact calculation). Similarly, we plot in Fig. 5(c), using blue solid and red dashed curves, the exact and analytical solutions for the high-frequency mode of the qubit  $f_{10}$  versus the normalized applied flux. The slight bending in the exact diagonalization curve (the solid blue), seen around 14 GHz, is due to the crossing of  $f_{10}$ , the first excited level of the SQUID oscillator, and the third level of the qubit.

## V. CALCULATION OF THE DECOHERENCE RATES

We now employ Fermi-golden-rule-type formulas in Eqs. (10) and (11) of Ref. [30] to calculate the relaxation and dephasing rates of the WTQ:

$$\frac{1}{T_1} = \frac{4}{\hbar} |\langle 0 | \bar{\mathbf{m}}^T \mathbf{f} | 1 \rangle|^2 J(\omega_{01}) \coth\left(\frac{\hbar\omega_{01}}{2k_B T}\right), \quad (74)$$

$$\frac{1}{T_\phi} = \frac{1}{\hbar} |\langle 0 | \bar{\mathbf{m}}^T \mathbf{f} | 0 \rangle - \langle 1 | \bar{\mathbf{m}}^T \mathbf{f} | 1 \rangle|^2 \frac{J(\omega)}{\hbar\omega} \Big|_{\omega \rightarrow 0} 2k_B T, \quad (75)$$

where  $\bar{\mathbf{m}}$  is the vector giving the coupling to the impedance in the final frame, that is

$$\begin{aligned} \bar{\mathbf{m}} &= \mathbf{R}_f^T \bar{\mathbf{m}}_0 \\ &= \begin{pmatrix} 0 \\ \frac{C_a C_b M_1}{\sqrt{C_{J_2} C_{\alpha,3} C_{\beta,3} L_1}} \\ \frac{(C'_1 + C_c) \sqrt{C_{J_3} M_1}}{\sqrt{C_A C_B C_{\alpha,3} C_{\beta,3} L_1}} - \sqrt{\frac{C_{\alpha,3} C_{\beta,3}}{C_A C_B C_{J_3} L_2}} M_2 \\ 0 \end{pmatrix}. \end{aligned} \quad (76)$$

Hence, we see that only the fast coordinates ( $f_2$  and  $f_3$ ) are coupled to the decoherence source, which is the impedance  $Z(\omega)$ .

The spectral density  $J(\omega)$  of the bath due to the impedance  $Z(\omega)$  is calculated using Eq. (93) of Ref. [29] (up to the scale factors)

$$J(\omega) = \text{Im}[K(\omega)] = \frac{\omega \text{Re}[Z(\omega)]}{\omega^2 L_c^2 + |Z|^2 + 2\omega L_c \text{Im}[Z(\omega)]}, \quad (77)$$

where  $K(\omega)$  is the kernel function of the bath given in Eq. (73) of Ref. [29] as

$$K(\omega) = \bar{\mathbf{L}}_Z^{-1}(\omega). \quad (78)$$



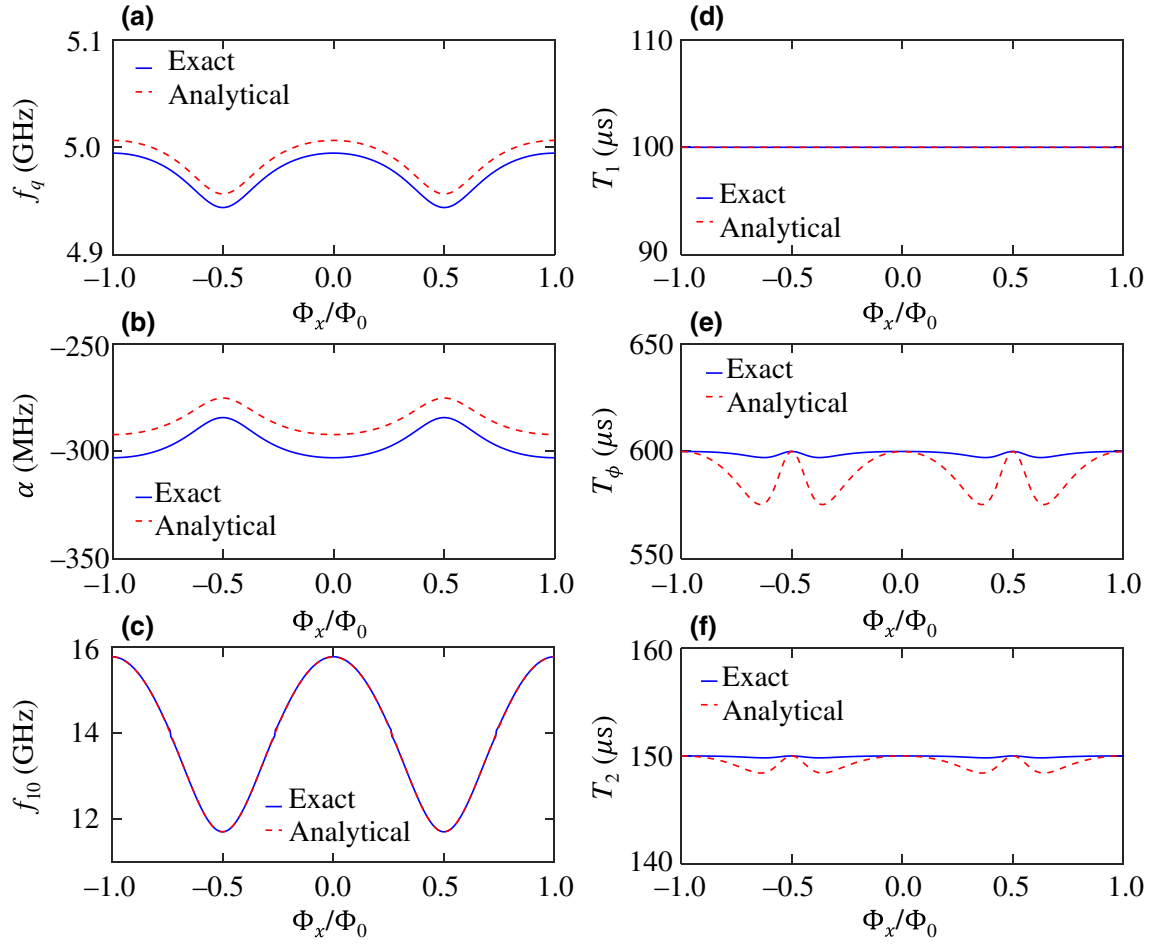


FIG. 5. A WTQ example. (a) Qubit frequency and (b) anharmonicity of the WTQ as a function of the normalized flux threading the SQUID loop. In this example, the WTQ has a maximum frequency and anharmonicity of about 5 GHz and 300 MHz, respectively, and exhibits a frequency tunability  $\delta = 50$  MHz. Blue curves are obtained by the diagonalization of the Hamiltonian in Eq. (60) in the charge basis. Red dashed curves are calculated using the analytical formulas in Eqs. (64) and (73). (c) The high-frequency mode of the WTQ  $f_{10}$  versus normalized flux. The WTQ circuit parameters employed in this example are  $I_{c1} = I_{c2} = 26$  nA,  $I_{c3} = \rho_J I_{c2}$ ,  $\rho_J = 3.5$ ,  $C_1 = 50$  fF,  $C_2 = 20$  fF,  $C_c = 20$  fF, where  $C_{J1} = C_{J2} = 1$  fF and  $C_{J3} = \rho_J C_{J2}$ . In plots (d)–(f), we evaluate the dependence of the WTQ coherence times, i.e.,  $T_1$ ,  $T_\phi$ , and  $T_2$  on the applied flux. In this calculation, we assume  $T = 0.02$  K and  $Z(\omega) = R = 0.1$  ohm and that the maximum values for  $T_1$  and  $T_2 = 1.5T_1$ , i.e.,  $100 \mu\text{s}$  and  $150 \mu\text{s}$ , respectively, are set by loss or noise sources that are independent of flux or the flux biasing circuit. The  $T_2$  curves in (f) are calculated using the relation  $1/T_2 = 1/2T_1 + 1/T_\phi$ , which also sets the maximum for  $T_\phi$  in (e). The analytical calculation of  $T_1$  and  $T_\phi$  uses the matrix element results of Eqs. (96)–(103). The exact calculation employs Eqs. (74) and (75) with a diagonalization of the Hamiltonian in Eq. (60).

$\tilde{\mathbf{L}}_Z$  is defined in Eq. (58) of Ref. [29] as

$$\tilde{\mathbf{L}}_Z = \mathbf{L}_{ZZ} - \mathbf{L}_{ZL}\mathbf{L}_{LL}^{-1}\mathbf{L}_{LZ}, \quad (79)$$

where  $\mathbf{L}_{ZZ}$  is given in Eq. (52) of Ref. [29] as

$$\mathbf{L}_{ZZ} = \mathbf{L}_Z + \mathbf{F}_{KZ}^T \tilde{\mathbf{L}}_K \mathbf{F}_{KZ} \quad (80)$$

$$= \mathbf{L}_Z + \tilde{\mathbf{L}}_K \quad (81)$$

$$= \frac{Z(\omega)}{i\omega} + L_c(1 - k_1^2 - k_2^2), \quad (82)$$

where in the second line above we use the fact that  $\mathbf{F}_{KZ} = 1$  and in the third line we use Eq. (14).  $\mathbf{L}_{ZL}$  is given by Eq.

(53) of Ref. [29] as

$$\mathbf{L}_{ZL} = \mathbf{F}_{KL}^T \tilde{\mathbf{L}}_K \mathbf{F}_{KZ} = 0, \quad (83)$$

since  $\mathbf{F}_{KL} = 0$ . Hence,  $\tilde{\mathbf{L}}_Z$  in Eq. (79) above is given by

$$\tilde{\mathbf{L}}_Z = \mathbf{L}_{ZZ} \quad (84)$$

$$= \frac{Z(\omega)}{i\omega} + L_c(1 - k_1^2 - k_2^2). \quad (85)$$

Now Eq. (78) for  $K(\omega)$  reads

$$K(\omega) = \bar{\mathbf{L}}_Z^{-1}(\omega) \quad (86)$$

$$= \frac{i\omega}{Z(\omega) + i\omega L_c(1 - k_1^2 - k_2^2)}. \quad (87)$$

Furthermore, calculating  $\text{Im}[K(\omega)]$  using Eq. (87) yields the result of Eq. (77) since  $k_1, k_2 \ll 1$ .

The dependence of the argument  $\bar{\mathbf{m}}^T \mathbf{f}$  of the matrix elements on the slow coordinates  $\varphi_1$  and  $\varphi_2$  can be calculated using Eqs. (16)–(20) of Ref. [30]. Equation (16) of Ref. [30] reads

$$(\mathbf{f}_\perp^{\min})(\mathbf{f}_\parallel) = -\frac{1}{2} \mathbf{b}^{-1} \mathbf{a}(\mathbf{f}_\parallel), \quad (88)$$

where  $(\mathbf{f}_\perp^{\min})(\mathbf{f}_\parallel)$  gives the dependence of the fast coordinates on the slow coordinates with

$$\mathbf{a}(\mathbf{f}_\parallel) = \begin{pmatrix} \alpha_{12} & \alpha_{22} & \alpha_{32} \\ \alpha_{13} & \alpha_{23} & \alpha_{33} \end{pmatrix} \begin{pmatrix} \sin(\varphi_{J_1})/L_{J_1} \\ \sin(\varphi_{J_2})/L_{J_2} \\ \sin(\varphi_{J_3})/L_{J_3} \end{pmatrix}. \quad (89)$$

Hence,

$$\bar{\mathbf{m}}^T \mathbf{f} = \bar{\mathbf{m}}_\perp^T (\mathbf{f}_\perp^{\min})(\mathbf{f}_\parallel) \quad (90)$$

$$= A_s^{(1)} \sin(\varphi_{J_1}) + A_s^{(2)} \sin(\varphi_{J_2}) + A_s^{(3)} \sin(\varphi_{J_3}), \quad (91)$$

where  $\bar{\mathbf{m}}_\perp$  is the subvector of  $\bar{\mathbf{m}}$  corresponding to the fast coordinates and

$$\mathbf{A}_s = \begin{pmatrix} A_s^{(1)} \\ A_s^{(2)} \\ A_s^{(3)} \end{pmatrix} = \begin{pmatrix} \frac{C_c(C_{J_2}M_1 - C_{J_3}M_2)}{C_a C_b L_{J_1}} \\ -\frac{C_{\alpha,3}C_{\beta,3}M_1 + (C_1 + C_c)C_{J_3}M_2}{C_a C_b L_{J_2}} \\ \frac{(C_1 + C_c)C_{J_2}M_1 + C_{\alpha,2}C_{\beta,2}M_2}{C_a C_b L_{J_3}} \end{pmatrix}. \quad (92)$$

Note that we drop the dc flux bias terms in the expression in Eq. (90) above. The last two terms in the above expression can again be combined in a single sine function as

$$\bar{\mathbf{m}}^T \mathbf{f} = A_s^{(1)} \sin(\varphi_1 + \varphi_{x,1}^{(0)}) + A \cos\left(\frac{\varphi_x}{2}\right) \sqrt{1 + d_s^2 \tan^2\left(\frac{\varphi_x}{2}\right)} \sin(\varphi_2 + \varphi_x^{(s)}), \quad (93)$$

where  $A = A_s^{(2)} + A_s^{(3)}$ ,  $d_s = (A_s^{(2)} - A_s^{(3)}) / (A_s^{(2)} + A_s^{(3)})$ , and  $\varphi_x^{(s)} = (\varphi_{x,2}^{(0)} + \varphi_{x,3}^{(0)}) / 2 + \tan^{-1}(d_s \tan(\varphi_x/2))$ .

Matrix elements can be evaluated by assuming harmonic wavefunctions for the main qubit mode and the SQUID mode. Since the coupling between the two modes

is dispersive, we can write the excited level  $|\tilde{1}\rangle$  of the qubit as

$$|\tilde{1}\rangle \approx \left(1 - \frac{\epsilon^2}{2}\right) |10\rangle - \epsilon |01\rangle, \quad (94)$$

where  $\epsilon = J_{12}/\Delta$ . Here the excitation on the left under the ket corresponds to the qubit mode, whereas the right excitation corresponds to the SQUID mode and  $\Delta = \omega_2 - \omega_1$  is the detuning between the qubit and SQUID modes. The coupling rate  $J_{12}$  between the qubit and SQUID mode is given by

$$J_{12} = \frac{1}{2\sqrt{Z_1 Z_2}} \frac{C_c}{C_1' C_2' + C_c(C_1' + C_2')}, \quad (95)$$

where  $Z_1$  is the characteristic impedance of the qubit mode and  $Z_2$  is the characteristic impedance of the SQUID mode, which are given by

$$Z_1 = \frac{1}{\omega_1(C_1' + C_c)},$$

$$Z_2 = \sqrt{\frac{L_{J_S}}{(C_2' + C_c)\left(1 - \frac{2EC_2}{\hbar\omega_2}\right)}}.$$

Using symmetry arguments one can show that

$$\langle \tilde{0} | \sin(\varphi_1 + \varphi_x^{(1)}) | \tilde{0} \rangle = 0, \quad (96)$$

$$\langle \tilde{1} | \sin(\varphi_1 + \varphi_x^{(1)}) | \tilde{1} \rangle = 0. \quad (97)$$

Using Eq. (94), we get

$$\langle \tilde{1} | \sin(\varphi_2 + \varphi_x^{(s)}) | \tilde{1} \rangle = \left(1 - \frac{\epsilon^2}{2}\right)^2 \langle 10 | \sin(\varphi_2 + \varphi_x^{(s)}) | 10 \rangle + \epsilon^2 \langle 01 | \sin(\varphi_2 + \varphi_x^{(s)}) | 01 \rangle. \quad (98)$$

Hence,

$$\begin{aligned} \langle 0 | \bar{\mathbf{m}}^T \mathbf{f} | 0 \rangle - \langle 1 | \bar{\mathbf{m}}^T \mathbf{f} | 1 \rangle &\approx \epsilon^2 \langle 10 | \sin(\varphi_2 + \varphi_x^{(s)}) | 10 \rangle \\ &\quad - \epsilon^2 \langle 01 | \sin(\varphi_2 + \varphi_x^{(s)}) | 01 \rangle \\ &= \epsilon^2 \eta_2^2 \exp\left(-\frac{\eta_2^2}{2}\right) \sin(\varphi_\Delta), \end{aligned} \quad (99)$$

where

$$\varphi_\Delta = \tan^{-1}\left(d \tan\left(\frac{\varphi_x}{2}\right)\right) + \tan^{-1}\left(d_s \tan\left(\frac{\varphi_x}{2}\right)\right), \quad (100)$$

$$\eta_2^2 = 4\pi \left(\frac{Z_2}{R_Q}\right), \quad (101)$$

and  $R_Q = \frac{\hbar}{e^2} \approx 25\,813\,\Omega$  is the resistance quantum.

The matrix elements in the  $T_1$  expression in Eq. (74) can be calculated as

$$\begin{aligned} \langle \widetilde{0} | \sin(\varphi_1 + \varphi_x^{(1)}) | \widetilde{1} \rangle &= \langle 00 | \sin(\varphi_1 + \varphi_x^{(1)}) | 10 \rangle \\ &= \eta_1 \exp\left(-\frac{\eta_1^2}{2}\right), \end{aligned} \quad (102)$$

with  $\eta_1^2 = 4\pi (Z_1/R_Q)$  and

$$\begin{aligned} \langle \widetilde{0} | \sin(\varphi_2 + \varphi_x^{(s)}) | \widetilde{1} \rangle &= \epsilon^2 \langle 00 | \sin(\varphi_2 + \varphi_x^{(s)}) | 01 \rangle \\ &= \epsilon^2 \eta_2 \exp\left(-\frac{\eta_2^2}{2}\right) \cos(\varphi_\Delta). \end{aligned} \quad (103)$$

Using the WTQ example of Figs. 5(a)–5(c), we compare in Figs. 5(d) and 5(e) the calculation for the relaxation and pure dephasing times as a function of normalized applied flux based on Eqs. (74) and (75) and the diagonalization of the Hamiltonian [Eq. (60)] versus the approximate results obtained using the analytical expressions for the matrix elements derived above, where in both cases we assume a constant, real impedance  $Z(\omega) = R$ . To complete the picture, we plot in Fig. 5(f) the expected decoherence time  $T_2$  for the same WTQ example given by the relation  $T_2^{-1} = (2T_1)^{-1} + T_\phi^{-1}$ . In our theoretical evaluation of the coherence times of the qubit, i.e.,  $T_1$ ,  $T_\phi$ , and  $T_2$ , we make the following assumptions: (1) the maximum relaxation time 100  $\mu\text{s}$  of the qubit is limited by a loss mechanism that is unrelated to the flux biasing source, such as dielectric loss. (2) The maximum decoherence time of the qubit  $T_2$  is equal to  $1.5T_1$  and limited by a nonflux noise source, such as thermal photon population in the readout resonator, which remains the dominant dephasing mechanism in our quantum processors. (3) The parameters  $R$  and  $T$  associated with the flux biasing circuit are 0.01 ohm and 0.1 K, respectively.

Furthermore, to illustrate the dependence of the dephasing time on the parameter  $R$  of the flux-biasing circuit for fixed  $T = 0.02$  K, we use the WTQ example of Fig. 5 and plot in Fig. 6(a) the exact solution of  $T_\phi$  versus normalized applied flux corresponding to varying parameter  $R$ . The blue, cyan, magenta, and red curves in Fig. 6(a) correspond to  $R = 1, 0.1, 0.05, 0.01$  ohm, respectively. As expected, we find that the dips in  $T_\phi$  away from the sweet spots increase with decreasing  $R$ . This is because the smaller the resistance in parallel with the current source is (see Fig. 3), the larger the current portion flowing through it.

Likewise, in Fig. 6(b), we illustrate the dependence of  $T_\phi$  on the parameter  $T$ , while keeping  $R = 0.1$  ohm constant. The blue, cyan, magenta, and red curves in Fig. 6(b) correspond to  $T = 0.02, 0.2, 0.4, 1$  K, respectively. As expected in this case as well, the dips in  $T_\phi$  away from the sweet spots increase with  $T$  of the flux-biasing circuit resistor that is in parallel with the current source (see Fig. 3).

## VI. EXPERIMENTAL RESULTS

We realize and measure two seven-qubit chips (referred to as  $A$  and  $B$ ), which are similar in design to those with single JJ transmons we measured in the past [17]. Each chip includes six WTQs and one single-JJ transmon as shown in the device photo in Fig. 7(a). Each qubit is capacitively coupled to a readout resonator, which, in turn, is capacitively coupled to a readout port. All resonator buses coupling the qubits are disabled by shorting their ends to ground. We implement the WTQs in two configurations, labeled P shape and U shape, which differ in the shape of the gap-capacitance electrodes shunting the JJs. In the P-shape configuration exhibited in Fig. 7(b), the three capacitance electrodes are parallel to each other, whereas in the U-shape configuration displayed in Fig. 7(c), one of the outer electrodes wraps around three sides of the middle electrode of the qubit. The motivation for designing

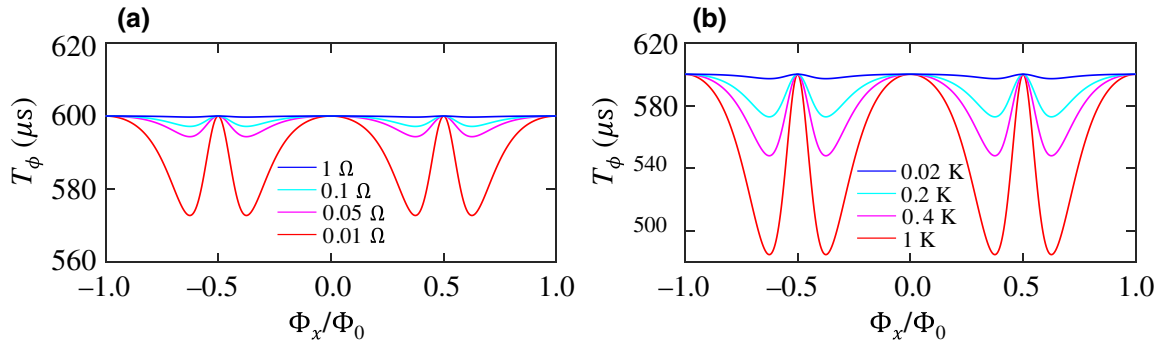


FIG. 6. Dependence of WTQ dephasing time  $T_\phi$  on the normalized flux threading the SQUID loop for varying parameter  $R$  (a) and  $T$  (b) of the flux biasing circuit, where  $Z(\omega) = R$  is assumed. In (a),(b) the values of  $T$  and  $R$  are set to 0.02 K and 0.1 ohm, respectively. The WTQ circuit parameters employed in this calculation are the same as Fig. 5. The curves in both plots are obtained by the diagonalization of the Hamiltonian in Eq. (60) in the charge basis along with Eqs. (74) and (75).

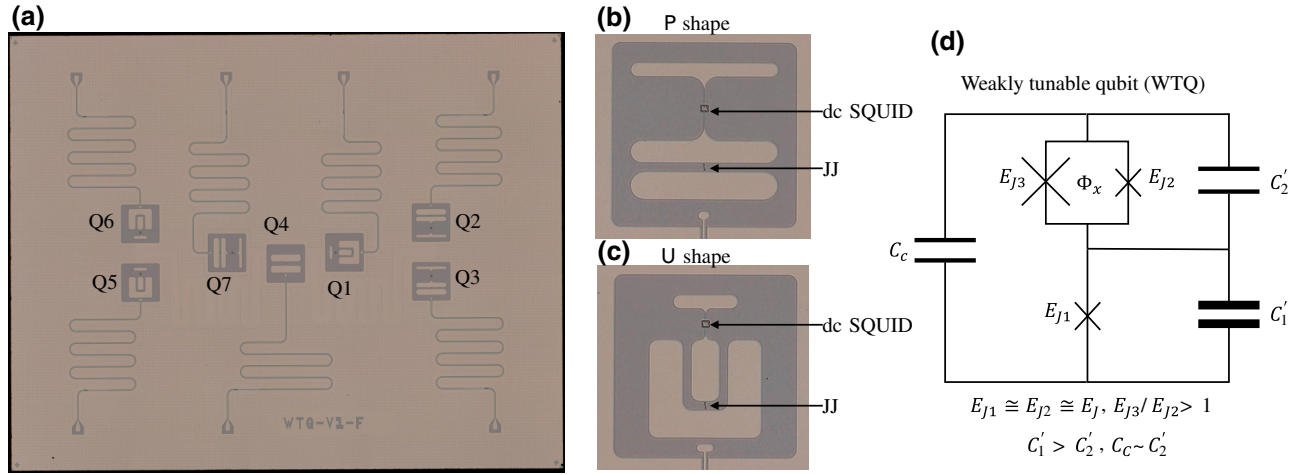


FIG. 7. (a) Photo of one of the two seven-qubit chips measured in this work. The chip consists of six WTQs and one single-JJ transmon (Q4). The WTQs are realized using two gap-capacitance geometries shown in (b),(c). (b) P-shape WTQ (Q2, Q3, Q7), in which the capacitance pads are parallel. (c) U-shape WTQ (Q1, Q5, Q6), in which one capacitance pad is curved. The fabrication of the WTQ chips follows the same planar device fabrication process described in Ref. [16]. (d) Equivalent WTQ circuit.  $C'_1$  and  $C'_2$  represent the total capacitance shunting the JJs (including the self capacitance of the JJs). The small junction of the SQUID is comparable to the junction of the single-JJ transmon  $E_{J2} \cong E_{J1} \cong E_J$ , whereas the other JJ of the SQUID is slightly larger, giving  $\rho_J = 2 - 5$ . Rounded corners used in the electrodes are an effort to minimize  $E$ -field concentration and are not specific to the WTQ design.

WTQs using these two possible configurations is to experimentally examine if either holds any coherence advantage over the other. In Fig. 7(d), we exhibit a simplified circuit of the WTQ. The shunting capacitances  $C'_1$ ,  $C'_2$  include the capacitances of the JJs. Figure 7(d) also outlines the useful parameter space of WTQ capacitances and Josephson energies (i.e., in comparison to the transmon qubits presented in Fig. 1).

The WTQ chips are mounted in a light-tight magnetic shield that has a top cover made of eccosorb. The input line incorporates cryogenic attenuators at different stages inside the fridge. The output line incorporates two wide-band isolators 4 – 12 GHz and a K&L filter with a cutoff at 12 GHz at the base temperature and a Caltech HEMT at the 4-K stage. Since the readout resonators are measured in reflection, we use a three-port 4–8 GHz cryogenic circulator at the bottom of the fridge to connect to the input line,

the output line, and to a microwave switch that allows us to measure the different readout and qubit devices on the quantum chip.

The magnetic flux is generated using a dc-current  $I_B$  applied to a small global superconducting coil with  $L_c \simeq 5.5$  mH attached to the device copper package. The mutual inductance  $M$  between the coil and the SQUID loops across the chip vary in the range 0.8–1.1 pH.

The leads of the small superconducting coil are soldered to a pair of normal metal pins located on the coil body. Those pins are connected to another set of normal metal pins embedded in the eccosorb cover via superconducting twisted pairs. Another set of superconducting twisted pairs connect the pins in the eccosorb to a first D connector at the mixing chamber. The dc wires that connect this first D connector to a second D connector at the 4-K stage are superconducting and resistive in the experiment of chip *A*

TABLE I. Measured parameters of chip *A*. Q4 is the single-JJ transmon on the chip. The SQUID JJ ratio parameter  $\rho_J$  is extracted from the spectroscopy fits.  $f_{01}^{\max}$  is the maximum measured qubit frequency.  $\alpha^{\max}$  ( $\alpha^{\min}$ ) is the maximum (minimum) measured anharmonicity obtained at  $f_{01}^{\max}$  ( $f_{01}^{\min}$ ).  $\delta$  is the measured frequency tunability range.  $T_{2E}^{\max}$  is the maximum measured coherence and  $T_1$  is the corresponding lifetime taken at the same flux bias. The coherence times for WTQ6 and WTQ7 are not measured.

Qubit	$\rho_J$	$f_{01}^{\max}$ (GHz)	$f_r$ (GHz)	$ \alpha ^{\max}$ (MHz)	$ \alpha ^{\min}$ (MHz)	$\delta$ (MHz)	$T_1$ ( $\mu$ s)	$T_{2E}^{\max}$ ( $\mu$ s)
WTQ1	2.6	4.8905	6.8869	254	224	99	75	85
WTQ2	3.5	4.57	6.9642	254	233	50	82	136
WTQ3	2.8	4.681	6.8372	246	215	89	64	65
Q4		5.0785	6.9567	360	360		65	36
WTQ5	3.5	4.442	6.9217	265	248	43	71	120
WTQ6	2.8	4.653	6.790	260	239	86	...	...
WTQ7	3.0	4.6065	6.867	252	226	76	...	...

TABLE II. Circuit parameters of chip *A* qubits extracted from the spectroscopy theory fits.

Qubit	Design	$\rho_S$	$C'_1$ (fF)	$C'_2$ (fF)	$C_c$ (fF)	$I_{c1}$ (nA)	$I_{c2}$ (nA)	$I_{c3}$ (nA)	$\rho_J$ (fit)
<b>WTQ1</b>	U	4.2	60.5	17.8	20.0	28.3	25.0	65.3	2.6
<b>WTQ2</b>	P	5.1	61	18.4	20.5	25.2	20.0	69.8	3.5
<b>WTQ3</b>	P	4.2	61	17.8	20.6	26.4	21.3	60	2.8
<b>Q4</b>			62.9			24.0			
<b>WTQ5</b>	U	5.1	60.0	18.4	20.0	23.4	20.2	70.7	3.5
<b>WTQ6</b>	U	4.2	60.7	18.3	20.1	25.9	21.3	60.0	2.8
<b>WTQ7</b>	P	4.2	60.0	18.1	20.7	25.4	20.0	60.2	3.0

and *B*, respectively. The remainder of the wires to the top of the fridge are resistive.

In what follows, we present the main results measured for chip *A* and *B*, whose circuit parameters are listed in Tables I and II for chip *A* and Tables III and IV for chip *B*. The WTQs in chip *A* yield a smaller  $\delta$  range 43–99 MHz (see Table I) versus 115–288 MHz (see Table III) for chip *B*, since they are designed with a slightly higher JJ area ratio of the SQUIDs, i.e.,  $\rho_S = A_{J_3}/A_{J_2}$ , where  $A_{J_2}$  and  $A_{J_3}$  represent the design area of the respective junctions. In chip *A*, we set  $\rho_S = 4.2$  for WTQ1, WTQ3, WTQ6, WTQ7, versus  $\rho_S = 2.9$  for the corresponding qubits in chip *B*, and  $\rho_S = 5.1$  for WTQ2 and WTQ5 in chip *A* versus  $\rho_S = 3.0$  in chip *B*. The two chips also differ in the JJ oxidation conditions applied in fabrication, yielding higher maximum WTQ frequencies for chip *B*, i.e., 5.5–5.97 GHz, than chip *A*, i.e., 4.44–4.89 GHz. Lastly, chips *A* and *B* are measured in two different cooldowns.

In Figs. 8(a)–8(d), we show spectroscopy measurements of WTQ2 (P shape), WTQ3 (P shape), WTQ5 (U shape), and WTQ6 (U shape) of chip *A*, respectively, plotted versus the normalized external flux threading the SQUID loop. The dashed black curves plotted over the data represent theoretical fits for the qubit frequency  $f_{01}$  and  $f_{02}/2$ . In Table II, we list the capacitance and critical current parameters of the various qubits used in the spectroscopy fits (including those of WTQ1 and WTQ7 whose data are not shown). The fits also allow us to extract the JJ asymmetry parameter of the dc SQUIDs  $\rho_J$  for the various qubits, which we list in Tables I and II for chip *A*. As expected

from the device physics, higher values of  $\rho_J$  correlate well with smaller observed  $\delta$  of the WTQs.

As seen in the figure, the maximum and minimum qubit frequencies are obtained at  $\Phi_x = 0$  and  $\Phi_x = \pm\Phi_0/2$ , respectively. The smallest  $\delta$  of 50 and 43 MHz are measured for WTQ2 and WTQ5, respectively, which are designed to have a slightly larger JJ asymmetry than WTQ3 and WTQ6, whose  $\delta$  is 89 and 86 MHz, respectively. Notably, the  $\rho_J$  extracted from the fits (see Table II), i.e., 3.5 and 2.8, match fairly well the dc resistance ratios measured for test JJs (fabricated on the same wafer) that have the same area ratios as the JJs of the SQUIDs.

Furthermore, using the spectroscopy data, we calculate the maximum and minimum magnitude of the WTQ anharmonicity given by  $|\alpha| = |f_{12} - f_{01}|$  at the upper and bottom sweet spots corresponding to  $\Phi_x = 0$  and  $\Phi_x = \pm\Phi_0/2$ , respectively (see Table I). For example, the anharmonicity of qubits with  $\delta$  of 43–99 MHz varies by 17–31 MHz.

Similarly, Table III summarizes the main figures of merit measured for qubits in chip *B*, while Table IV lists the capacitance and critical current parameters of the various qubits in chip *B* extracted from their corresponding spectroscopy fits (not shown).

In Figs. 9 and 10, we plot the measured coherence times for qubits in chip *A* and chip *B*, respectively. In Fig. 9, the columns, from left to right, represent the results of the single-JJ transmon Q4 (a), WTQ2 (b), WTQ3 (c), and WTQ5 (d). The rows, from top to bottom, display the qubit frequency  $f_q$ , relaxation time  $T_1$ , decoherence times  $T_{2E}$  (echo) and  $T_{2R}$  (Ramsey), and extracted dephasing time

TABLE III. Measured parameters of chip *B*. Q4 is a single-JJ transmon. WTQ1 did not yield (one of its SQUID junctions is open). The SQUID JJ ratio parameter  $\rho_J$  is extracted from the spectroscopy fits.  $f_{01}^{\max}$  is the maximum measured qubit frequency.  $\alpha^{\max}$  ( $\alpha^{\min}$ ) is the maximum (minimum) measured anharmonicity obtained at  $f_{01}^{\max}$  ( $f_{01}^{\min}$ ).  $\delta$  is the measured frequency tunability range.  $T_{2E}^{\max}$  is the maximum measured coherence and  $T_1$  is the corresponding lifetime taken at the same flux bias. The relatively low  $T_1$  of Q4 is limited by the Purcell effect due to the proximity of  $f_{01}$  to the readout frequency.

Qubit	$\rho_J$	$f_{01}^{\max}$ (GHz)	$f_r$ (GHz)	$ \alpha ^{\max}$ (MHz)	$ \alpha ^{\min}$ (MHz)	$\delta$ (MHz)	$T_1$ ( $\mu$ s)	$T_{2E}^{\max}$ ( $\mu$ s)
<b>WTQ2</b>	2.36	5.6805	6.9683	252	224	115	42	40
<b>WTQ3</b>	2.06	5.557	6.8410	243	189	207	57	33
<b>Q4</b>		6.375	6.967	349	349		13	25
<b>WTQ5</b>	2.06	5.497	6.9262	250	161	159	47	73
<b>WTQ6</b>	1.9	5.743	6.7906	248	181	287	40	58
<b>WTQ7</b>	1.95	5.972	6.869	226	162	262	29	42

TABLE IV. Circuit parameters of chip *B* qubits extracted from the spectroscopy theory fits. WTQ1 on chip *B* is not measured because one of its SQUID junctions did not yield (open).

Qubit	Design	$\rho_S$	$C'_1$ (fF)	$C'_2$ (fF)	$C_c$ (fF)	$I_{c1}$ (nA)	$I_{c2}$ (nA)	$I_{c3}$ (nA)	$\rho_J$ (fit)
WTQ2	P	3	61.4	18.3	20.0	37.9	40.0	94.4	2.36
WTQ3	P	2.9	61.5	18.5	20.7	36.9	36.0	74	2.06
Q4			62.9			36.7			
WTQ5	U	3	61.4	18.0	20.0	35.7	40.0	82.4	2.06
WTQ6	U	2.9	60.3	18.3	20.0	38.5	38.0	72.0	1.9
WTQ7	P	2.9	60.1	18.0	20.7	42.0	41.0	80.0	1.95

given by  $T_\varphi^{-1} = T_{2E}^{-1} - (2T_1)^{-1}$ , plotted as a function of  $I_B$ , i.e., the direct current applied to the global coil flux biasing the qubits.

The solid black curves in the first row plots represent theory fits based on the diagonalization of the WTQ Hamiltonian. The solid blue curves in the second row plots represent theory fits for  $T_1$  calculated using Eq. (74). The upper bound of these fits is set to match the experimental data [typically  $T_1$  that corresponds to the maximum  $T_{2E}$ , listed in Table I (for chip *A* and Fig. 9) and Table III (for chip *B* and Fig. 10)]. The average  $T_1$  of the WTQs is similar to that of the fixed-frequency transmon Q4. This is consistent with the assumption that surface dielectric loss dominates relaxation in both the WTQ and the single-JJ transmon. Variations with flux as seen, for instance, in chip *A*, WTQ5 (Fig. 9) also suggest frequency-dependent couplings to TLSs. However we did

not explore this behavior systematically as was done in Ref. [22].

One observation regarding the measured  $T_{2E}$  (red circles) and  $T_{2R}$  (magenta squares) plotted in the third row and  $T_\varphi$  (blue circles) drawn in the fourth row of Fig. 9, is that they exhibit a pronounced decrease with  $|I_B|$ , which strongly indicates that the decoherence times in our system are primarily limited by heating effects caused by large  $|I_B|$ . This observation is further supported by the fact that we observe a rise in the temperature of the mixing chamber stage by several millikelvin during the lengthy data taking process of  $f_q$ ,  $T_1$ ,  $T_{2R}$ ,  $T_{2E}$  as  $I_B$  is swept (about 15 min for each  $I_B$ ). Another supporting evidence of the heating effect we observe in our system, is the monotonic decrease in  $T_{2R}$ ,  $T_{2E}$ , and  $T_\varphi$  of the single JJ transmon (Q4) (see the first column plots), which to a large extent is insensitive to flux noise.

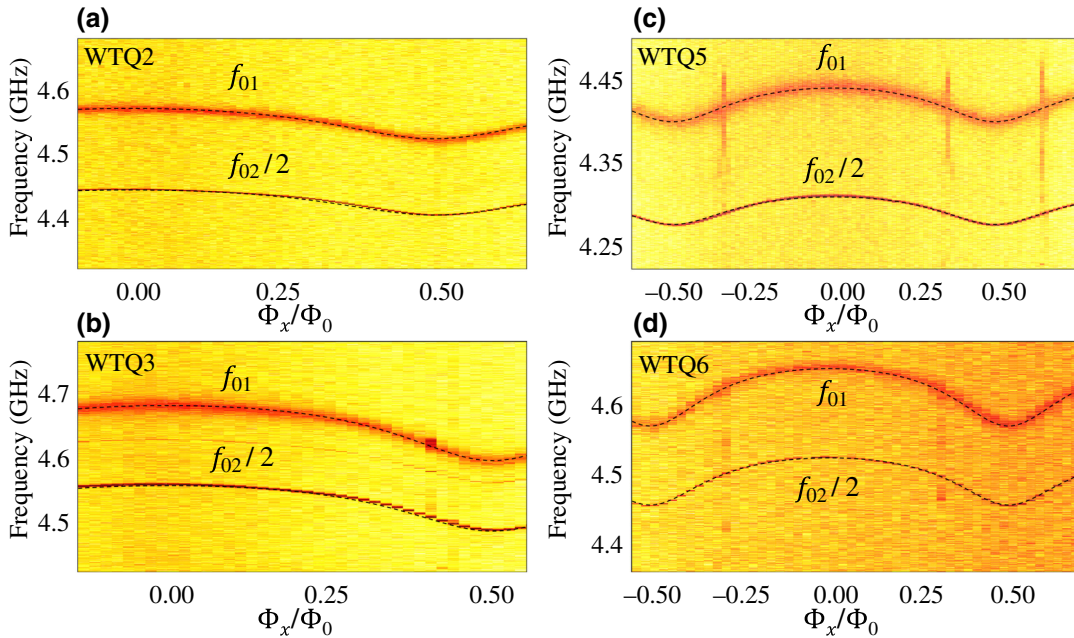


FIG. 8. Representative qubit spectroscopy measurements of chip *A* plotted versus normalized external flux. The data shows  $f_{01}$ , and  $f_{02}/2$  curves. (a) WTQ2 (P shape). (b) WTQ3 (P shape). (c) WTQ5 (U shape). (d) WTQ6 (U shape). WTQ2 and WTQ5, having  $\rho_J = 3.5$ , exhibit a small tunability of 50 MHz and 43 MHz, respectively. WTQ3 and WTQ6, having  $\rho_J = 2.8$ , exhibit a slightly larger tunability of 89 and 86 MHz. Dashed black curves are solutions to the Hamiltonian in Eq. (60).

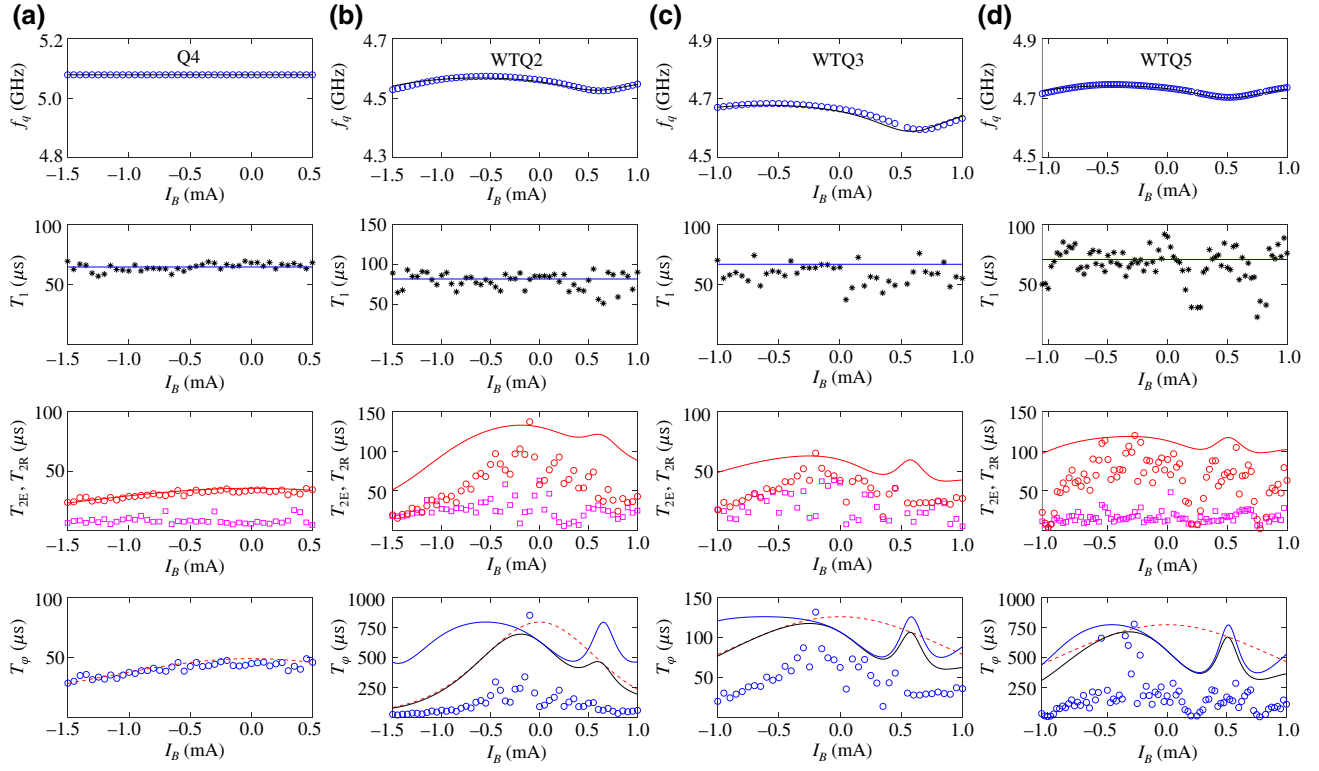


FIG. 9. Coherence measurements for chip *A* taken for Q4 (a), WTQ2 (b), WTQ3 (c), and WTQ5 (d). Top to bottom rows show the qubit frequency  $f_q$  (blue circles),  $T_1$  (black stars),  $T_{2E}$ ,  $T_{2R}$  (red circles and magenta squares, respectively), and  $T_\phi$  (blue circles) as a function of the applied coil bias current  $I_B$ . The solid black curves in the first row plots represent theory fits for the qubit frequency based on the diagonalization of the Hamiltonian. The solid blue curves drawn in the second row plots, represent fits based on Eq. (74). The solid red curves shown in the third row plots correspond to the calculated  $T_{2E}$  based on the  $T_1$  and  $T_\phi$  fits (see main text). The dashed red, solid blue, and solid black curves shown in the fourth row plots represent the calculated  $T_{\phi,D}$ ,  $T_{\phi,F}$ , and  $T_\phi$  fits, respectively (see main text and Table V for details). The observed maximum in  $T_\phi$  of WTQs seen in fourth row plots around  $-0.25$  mA can be attributed to the increase of  $T_{\phi,F}$  near the net zero flux bias around  $-0.5$  mA (that cancels the nonzero stray magnetic field in the setup), and the decrease of  $T_{\phi,D}$  due to the increase in the applied current magnitude responsible for heating.

To model the dependence of the dephasing time on heating caused by  $|I_B|$ , we consider one of the dominant dephasing mechanisms in qubits that are dispersively coupled to readout resonators, which arise from fluctuation in the qubit frequency due to thermal photon population in the readout resonator [36]. In the limit  $\bar{n} \ll 1$ , the dephasing rate associated with this mechanism (denoted  $\Gamma_{\phi,D} \equiv T_{\phi,D}^{-1}$ ) is given by [37]

$$\Gamma_{\phi,D} = \Gamma_c \bar{n}, \quad (104)$$

where  $\Gamma_c \equiv \kappa \chi^2 / (\kappa^2 + \chi^2)$ ,  $\kappa$  is the total photon decay rate of the fundamental mode of the readout resonator with angular frequency  $\omega_r = 2\pi f_r$  (here  $\kappa$  is dominated by the coupling rate to the external feedline),  $\chi$  is the qubit-state-dependent frequency shift of the readout resonator, and  $\bar{n}$  is the average thermal photon number in the resonator, where  $\bar{n} = 1 / (e^{\hbar\omega_r/k_B T_e} - 1)$  is the Bose-Einstein population of the 50-ohm external feedline (heat bath) at effective temperature  $T_e$ , which we express as  $T_e = \bar{T}_e + \delta T$ , where  $\bar{T}_e$  is the effective temperature with no bias current ( $I_B = 0$ ) and

$\delta T = \Theta I_B^2$  represents the rise in the effective temperature of the device due to ohmic dissipation.

Note that  $\delta T$  can be expressed as  $\delta T = C_H Q_d$ , where  $C_H$  is the heat capacity of the device and  $Q_d = R I_B^2 \tau_B / 2$  is the dissipated heat energy in the flux biasing circuit, the experimentally relevant temperature-to-current conversion coefficient  $\Theta$  can be expressed as  $\Theta = R C_H \tau_B / 2$ , where  $\tau_B$  is an effective measurement duration. In our qubit experiments, we find that  $\Theta$  varies in the range 5–10 mK/(mA)<sup>2</sup> for chip *A* (see Table V) and 3–7 mK/(mA)<sup>2</sup> for chip *B* (see Table VI).

The dashed red curves in the fourth row plots of Fig. 9 represent the calculated  $T_{\phi,D}$  for Q4 (a), WTQ2 (b), WTQ3 (c), and WTQ5 (d). Similarly, the solid blue curves represent the calculated dephasing time  $T_{\phi,F}$  that is set by the flux noise of the biasing circuit given by  $T_{\phi,F}^{-1} = T_\phi^{-1} + T_{\phi,D_0}^{-1}$ , where  $T_\phi$  is evaluated using Eq. (75) with  $T = \bar{T}_m + \delta T$ , where  $\bar{T}_m$  is the effective temperature of the superconducting magnetic coil with no bias current, and  $T_{\phi,D_0}$  is an experimental bound on dephasing time due to

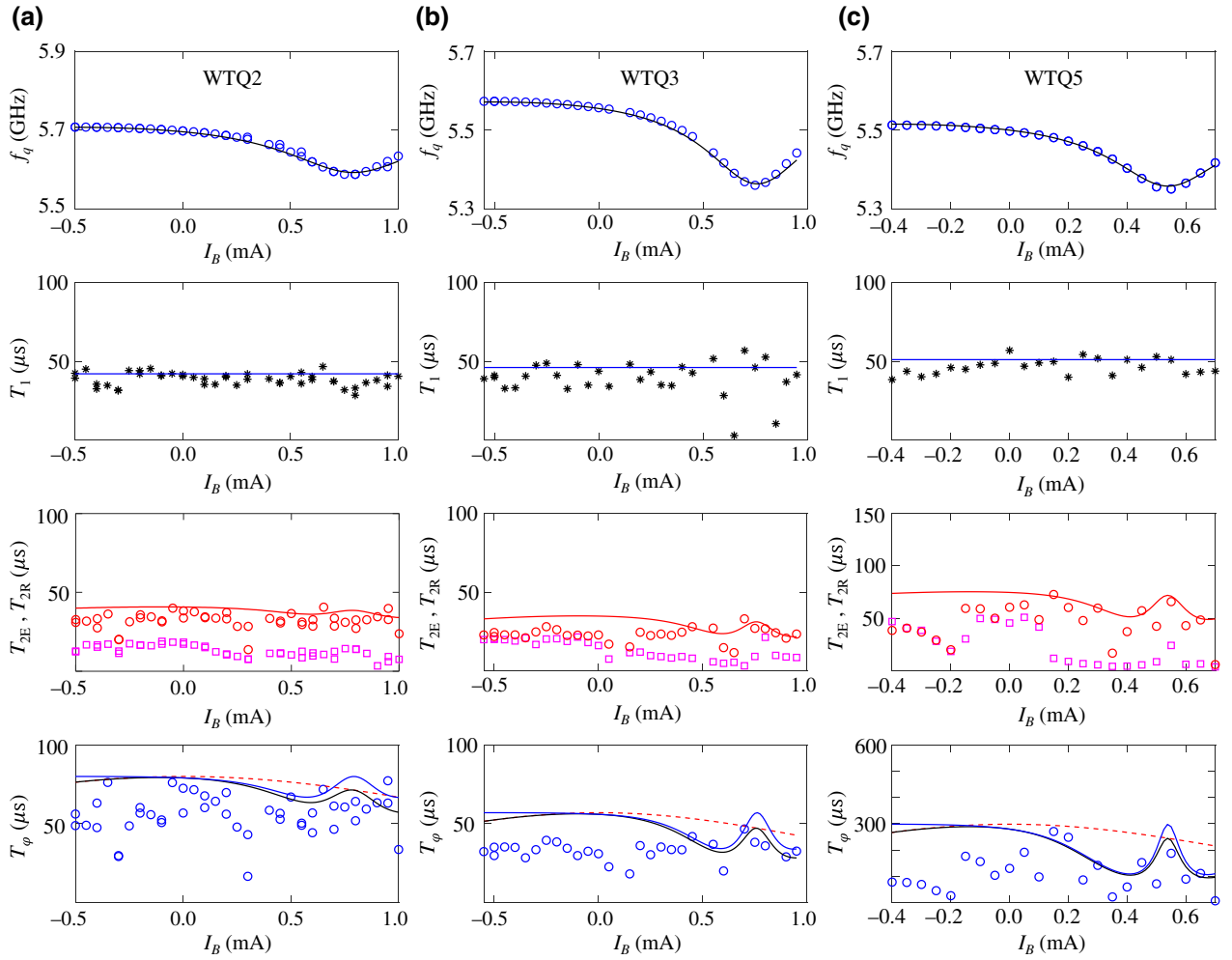


FIG. 10. Coherence measurements for chip *B* taken for WTQ2 (a), WTQ3 (b), and WTQ5 (c). Top to bottom rows show the qubit frequency  $f_q$  (blue circles),  $T_1$  (black stars),  $T_{2E}$ ,  $T_{2R}$  (red circles and magenta squares, respectively), and  $T_\phi$  (blue circles) as a function of the applied coil bias current  $I_B$ . The solid black curves in the first row plots represent theory fits for the qubit frequency based on the diagonalization of the Hamiltonian. The solid blue curves drawn in the second row plots, represent fits based on Eq. (74). The solid red curves shown in the third row plots correspond to the calculated  $T_{2E}$  based on the  $T_1$  and  $T_\phi$  fits (see main text). The dashed red, solid blue, and solid black curves shown in the fourth row plots represent the calculated  $T_{\phi,D}$ ,  $T_{\phi,F}$ , and  $T_\phi$  fits, respectively (see main text and Table VI for details).

the dispersive coupling mechanism. It is worth noting that heating has a lesser effect on  $T_{\phi,F}$  (solid blue curves) than  $T_{\phi,D}$  (dashed red curves). In the former case, heating causes the periodic response of  $T_\phi$  to decrease with  $|I_B|$ . Likewise, the solid black curves, drawn in the fourth row plots, represent the total dephasing time calculated using the relation  $T_\phi^{-1} = T_\phi^{-1} + T_{\phi,D}^{-1}$ , which accounts for the contribution of

both dephasing mechanisms discussed above and exhibits a fair agreement with the data.

Finally, we plot a bound on  $T_{2E}$ , drawn as solid red curves in the third row plots of Fig. 9, using the calculated  $T_\phi$  and the relation  $T_{2E}^{-1} = (2T_1)^{-1} + T_\phi^{-1}$ .

In a similar manner, in Fig. 10 we plot using the same symbols and conventions of Fig. 9 tunability curves and

TABLE V. Parameters of chip *A* qubits used in the coherence measurement theory fits shown in Fig. 9.

Qubit	$\kappa/2\pi$ (MHz)	$\chi/2\pi$ (MHz)	$\bar{T}_e$ (mK)	$\Theta$ mK/(mA) <sup>2</sup>	$\bar{T}_m$ (K)	$R$ ( $m\Omega$ )
<b>WTQ2</b>	0.45	0.47	47	10	0.2	1
<b>WTQ3</b>	0.65	0.39	67	7	0.2	1
<b>Q4</b>	0.82	0.51	78	5	0.2	1
<b>WTQ5</b>	0.65	0.26	55	5	0.2	1



TABLE VI. Parameters of chip  $B$  qubits used in the coherence measurement theory fits shown in Fig. 10.

Qubit	$\kappa/2\pi$ (MHz)	$\chi/2\pi$ (MHz)	$\bar{T}_e$ (mK)	$\Theta$ mK/(mA) <sup>2</sup>	$\bar{T}_m$ (K)	$R$ (m $\Omega$ )
<b>WTQ2</b>	0.6	0.4	74	3	0.1	2
<b>WTQ3</b>	0.5	0.63	70	5	0.1	2
<b>WTQ5</b>	0.65	0.39	58	7	0.05	2

coherence time measurements taken for qubits WTQ2 (a), WTQ3 (b), and WTQ5 (c) of chip  $B$  as a function of  $I_B$  and the corresponding theoretical fits.

## VII. DISCUSSION

As seen in Figs. 9 and 10, the WTQs exhibit coherence times, i.e.,  $T_1$  and  $T_\phi$ , that are comparable to those of single-JJ transmons fabricated on the same chip. These times are consistent with the loss and dephasing mechanisms typically seen in single-junction transmons, i.e., surface dielectric loss [38] and dispersive coupling in the case of  $T_\phi$  near the sweet spots (see the solid blue curves in the fourth row of Figs. 9 and 10).

We attribute the larger than expected drop in the measured  $T_\phi$  of the WTQs and transmons, observed for large  $|I_B|$  (see blue circles), to the unintended heating side effect produced by our flux biasing circuit as  $|I_B|$  is varied. This undesired heating effect is extrinsic to the qubits and can, in principle, be mitigated by careful engineering. For instance, windings in a superconducting coil can be made to extend into extra-long leads so that all resistive joints are made at higher-temperature stages of the cryostat, with careful thermal anchoring. Or, on-chip superconducting flux lines can be designed to individually bias each qubit via a high mutual inductance so that only a very small current is needed. Such biasing would require careful design of feedline wiring to minimize nonsuperconducting links to the chip, and incorporate proper filtering to avoid dephasing from instrumentation noise.

It is worthwhile to emphasize that the resistance of the flux biasing circuit affects the two dephasing mechanisms associated with our devices differently as reflected in the theoretical results of Fig. 6(a) and the experimental data in Figs. 9 and 10. As seen in Fig. 6(a) a higher resistance dampens the swings of the dephasing times at and away from the flux sweet spots, whereas higher resistance would increase the heating effect as seen in the experiment for large  $|I_B|$ . However, by applying some of the techniques outlined above, it should be possible to resolve this trade-off by reducing the heating effect in future systems.

While we do not observe flux-noise-limited dephasing in our experiment, we can estimate its effects. So-called “universal” flux noise with an approximately  $1/f$  power spectrum has been widely observed in superconducting systems. Its amplitude  $A_\phi^{1/2}$  at 1 Hz generally

exceeds  $1\mu\Phi_0$  and can be sensitive to SQUID loop geometry [39–41]. Following Ref. [19], we can write an approximate Ramsey dephasing rate  $\Gamma_{\phi,R} = |df_q/d\Phi_x| \times 2\pi\sqrt{A_\phi}|\ln(2\pi f_{IR}t)|$ , where  $f_{IR}$  is a cutoff frequency of 1 Hz, and  $t$  being on the order of  $1/\Gamma_{\phi,R}$  we take to be 10  $\mu$ s. We can find the flux sensitivity  $|df_q/d\Phi_x|$  as a function of flux by differentiating Eq. (64) with respect to flux. For example, for the qubits on chip  $A$ , we can use circuit parameters in Table II and differentiate numerically in terms of fractional flux quantum, with units of GHz/ $\Phi_0$ , as shown in Fig. 11(a). If we conservatively assume  $A_\phi^{1/2} \sim 2\mu\Phi_0$ , and taking the echoed dephasing rate  $\Gamma_{\phi,E}$  according to Ref. [42] to be  $\Gamma_{\phi,E} \sim 1/4\Gamma_{\phi,R}$ , and neglecting the contribution of qubit relaxation, we can estimate a lower bound for flux-noise-limited dephasing time

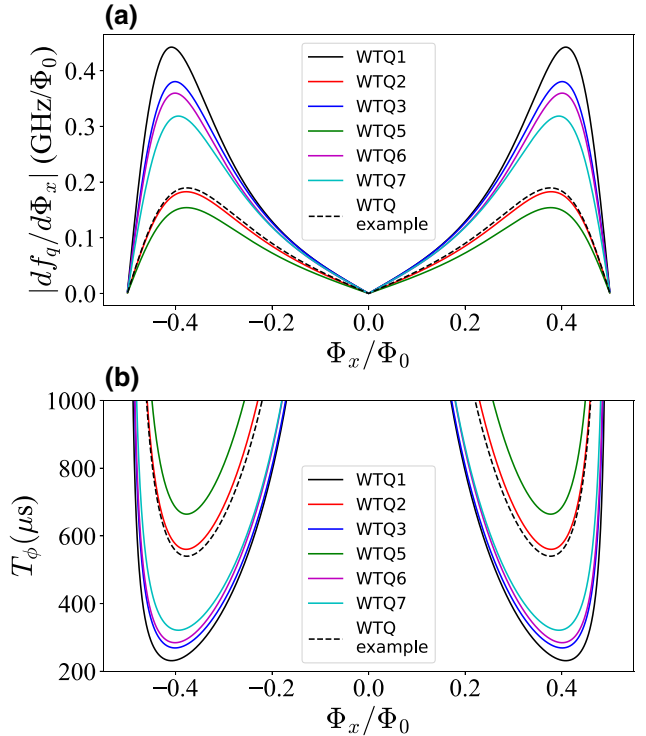


FIG. 11. (a) WTQ flux sensitivities of qubits on chip  $A$  and of example device, found by numerical differentiation of Eq. (64), using device parameters listed in Table II and Fig. 5. (b) Flux-noise-limited dephasing times  $T_\phi$ , assuming  $1/f$  flux-noise amplitude  $A_\phi^{1/2} \sim 2\mu\Phi_0$  at 1 Hz.

$T_\phi \sim 1/\Gamma_{\phi,E}$ . These dephasing times, shown in Fig. 11 (b) compare favorably to  $T_2^e = 200 \mu\text{s}$ , which is projected to be the minimum necessary to achieve fidelity  $\geq 99.9\%$  in cross-resonance gates [20]. The minimum dephasing times are comparable to the best average transmon dephasing times demonstrated in multiqubit devices [43]. Using the example parameters of Fig. 5 we find a minimum flux-noise-limited dephasing time comparable to the dephasing times presented in Figs. 5 and 6.

It is worth noting that we do not observe an obvious advantage for either the P or U WTQ designs with respect to the measured relaxation time  $T_1$  of the various qubits in both chips (or at least not in the range 50–100  $\mu\text{s}$  measured in the experiment).

It is also worth noting that, like single-JJ transmons, it is possible to adjust the maximum frequency of WTQs using focused laser beams following fabrication and JJ resistance measurement at room temperature [14]. WTQs are suitable for this technique because (1) the maximum frequency of WTQs is strongly dependent on the critical current of the non-SQUID JJ, and (2) the non-SQUID JJ of WTQs is physically well separated from the SQUID in both designs, thus it may be annealed without considerably affecting the SQUID JJs. Such a capability further enhances the ability of WTQs to avoid frequency collisions in large quantum systems as laser annealing can be selectively applied to WTQs across the chip (whose resistances are far off from their designed values), followed by, as necessary, an *in situ* fine tuning using applied flux when the device is cold. Hence, selective laser anneal may be combined with *in situ* flux tuning of WTQs to evade frequency collisions in large lattices of qubits, while maintaining high coherence. To quantify the effect on frequency crowding, we can adopt the simplified model [14] that a “collision-free” device of  $N$  qubits requires every qubit to lie within a “window”  $\pm\Delta f$  of its frequency set point. For normally distributed scatter at frequency precision  $\sigma_f$ , the likelihood of this occurring is found as the cumulative distribution function of  $\Delta f/\sigma_f$ , raised to the power  $N$ . For the conditions described in Ref. [14], a heavy-hexagon-type lattice of  $N = 1000$  qubits has  $\Delta f = 26$  MHz. WTQ tunability  $\delta$ , however, in practice enlarges this “window” by  $\delta/2$ . Taking the precision  $\sigma_f = 18$  MHz shown for multiqubit lattices in Ref. [15], we estimate that a 1000-qubit lattice made of WTQs of tunability  $\delta = 50$  MHz can be made collision-free 10% of the time, while using WTQs of tunability  $\delta = 99$  MHz gives a collision-free yield of 99%.

Our study of the WTQ suggests several areas for further investigation. (1) Measuring the dependence of higher modes of the WTQ on applied flux, in particular, the  $f_{10}$  mode that is theoretically calculated for the WTQ example of Fig. 5(c). (2) Demonstrating cross-resonance gates in multiqubit chips of WTQs and showing that frequency collisions can be avoided by applying independent fluxes

to neighboring qubits. (3) Finding out the limits on the tunability ranges that can be experimentally achieved with these qubits. (4) Interrogating TLS spectra in the frequency and time domains by flux tuning a WTQ.

## VIII. CONCLUSION

We introduce weakly tunable superconducting qubits whose frequency can be tuned with external magnetic flux. The qubits comprise capacitively shunted JJ and asymmetric dc SQUID, sharing one electrode and capacitively coupled via the other two.

We develop a theoretical model that captures the device physics and its coupling to the flux biasing circuit. By solving the full Hamiltonian of the system, we calculate the various qubit properties as a function of the circuit parameters and applied flux. We also calculate the qubit relaxation and dephasing times associated with the flux-biasing circuit. Furthermore, we derive analytical expressions that yield approximate values for the various device parameters and coherence times.

Moreover, we fabricate and test two superconducting chips containing several variations of these qubits. We show that they can achieve frequency tunability ranges as low as 43–287 MHz with only a small asymmetry in the size of their SQUID JJs ( $\rho_J = 2 - 3.5$ ), which are considerably lower than what is possible using highly asymmetric dc-SQUID transmons (about 350 MHz of tunability with an asymmetry factor of 15). Using such weakly flux-tunable qubits should enable us to resolve most common frequency collisions in multiqubit architectures while minimizing sensitivity to flux noise. For example, a 1000-qubit device comprising WTQs of tunability  $\delta = 50$  MHz and trimmed using laser anneal could achieve collision-free yield of 10% and dephasing times  $> 500 \mu\text{s}$ , while WTQs of tunability  $\delta = 99$  MHz could achieve collision-free yield of 99% and dephasing times  $> 200 \mu\text{s}$ . Furthermore, in any large qubit lattice it is likely that several qubits will suffer degraded coherence due to TLS coupling. WTQ tunability can restore the qubits’  $T_1$  and permit periodic adjustments if the TLSs drift over time [22].

These qubits also retain the key properties that have made transmons useful in multiqubit architectures, such as having 0-1 transition frequencies in the range 4–5.5 GHz, anharmonicities around 250–300 MHz, comparable relaxation and decoherence times to single-JJ transmons, small footprints, and a standard fabrication process. Moreover, because the WTQ has a transmon-type electromagnetic mode, we expect it to function in circuit architectures that support transmons, for instance, cross-resonance gates or other two-qubit gates that rely on transmission-line resonator coupling. In this way, the WTQ can be a tool to solve frequency-crowding issues in scaled-up quantum computing circuits.

## ACKNOWLEDGMENTS

B.A., J.B.H. thank Malcolm Carroll, Easwar Magesan, and Jay Gambetta for fruitful discussions. B.A. highly appreciates Jim Rozen's help with wiring the dilution fridge. This work is partially funded by the IARPA Grant No. W911NF-16-1-0114-FE. Contribution of the U.S. Government, not subject to copyright.

- 
- [1] P. W. Shor, Polynomial-time algorithms for prime factorization and discrete logarithms on a quantum computer, *SIAM J. Sci. Statist. Comput.* **26**, 1484 (1997).
- [2] N. Moll, P. Barkoutsos, L. S. Bishop, J. M. Chow, A. Cross, D. J. Egger, S. Filipp, A. Fuhrer, J. M. Gambetta, and M. Ganzhorn, Quantum optimization using variational algorithms on near-term quantum devices, *Quantum Sci. Technol.* **3**, 030503 (2018).
- [3] A. Kandala, A. Mezzacapo, K. Temme, M. Takita, M. Brink, J. M. Chow, and J. M. Gambetta, Hardware-efficient variational quantum eigensolver for small molecules and quantum magnets, *Nature* **549**, 242 (2017).
- [4] A. W. Cross, L. S. Bishop, S. Sheldon, P. D. Nation, and J. M. Gambetta, Validating quantum computers using randomized model circuits, *Phys. Rev. A* **100**, 032328 (2019).
- [5] A. G. Fowler, M. Mariantoni, J. M. Martinis, and A. N. Cleland, Surface codes: Towards practical large-scale quantum computation, *Phys. Rev. A* **86**, 032324 (2012).
- [6] E. Dennis, A. Kitaev, A. Landahl, and J. Preskill, Topological quantum memory, *J. Math. Phys.* **43**, 4452 (2002).
- [7] J. Koch, T. M. Yu, J. Gambetta, A. A. Houck, D. I. Schuster, J. Majer, A. Blais, M. H. Devoret, S. M. Girvin, and R. J. Schoelkopf, Charge-insensitive qubit design derived from the Cooper pair box, *Phys. Rev. A* **76**, 042319 (2007).
- [8] H. Paik, D. I. Schuster, L. S. Bishop, G. Kirchmair, G. Catelani, A. P. Sears, B. R. Johnson, M. J. Reagor, L. Frunzio, and L. I. Glazman, *et al.*, Observation of High Coherence in Josephson Junction Qubits Measured in a Three-Dimensional Circuit QED Architecture, *Phys. Rev. Lett.* **107**, 240501 (2011).
- [9] C. Rigetti, Jay M. Gambetta, S. Poletto, B. L. T. Plourde, J. M. Chow, A. D. Córcoles, J. A. Smolin, S. T. Merkel, J. R. Rozen, and G. A. Keefe, *et al.*, Superconducting qubit in a waveguide cavity with a coherence time approaching 0.1 ms, *Phys. Rev. B* **86**, 100506(R) (2012).
- [10] C. Rigetti and M. Devoret, Fully microwave-tunable universal gates in superconducting qubits with linear couplings and fixed transition frequencies, *Phys. Rev. B* **81**, 134507 (2010).
- [11] J. M. Chow, A. D. Córcoles, J. M. Gambetta, C. Rigetti, B. R. Johnson, J. A. Smolin, J. R. Rozen, G. A. Keefe, M. B. Rothwell, M. B. Ketchen, and M. Steffen, Simple All-Microwave Entangling Gate for Fixed-Frequency Superconducting Qubits, *Phys. Rev. Lett.* **107**, 080502 (2011).
- [12] A. P. M. Place, L. V. H. Rodgers, P. Mundada, B. M. Smitham, M. Fitzpatrick, Z. Leng, A. Premkumar, J. Bryon, A. Vrajitoarea, and S. Sussman, *et al.*, New material platform for superconducting transmon qubits with coherence times exceeding 0.3 milliseconds, *Nat. Commun.* **12**, 1779 (2021).
- [13] S. Sheldon, E. Magesan, J. M. Chow, and J. M. Gambetta, Procedure for systematically tuning up cross-talk in the cross-resonance gate, *Phys. Rev. A* **93**, 060302(R) (2016).
- [14] J. B. Hertzberg, E. J. Zhang, S. Rosenblatt, E. Magesan, J. A. Smolin, J.-Bang Yau, V. P. Adiga, M. Sandberg, M. Brink, J. M. Chow, and J. S. Orcutt, Laser-annealing Josephson junctions for yielding scaled-up superconducting quantum processors, *npj Quant. Info.* **7**, 129 (2021).
- [15] E. Zhang, S. Srinivasan, N. Sundaresan, D. F. Bogorin, Y. Martin, J. B. Hertzberg, J. Timmerwilke, E. J. Pritchett, J.-B. Yau, and C. Wang, *et al.*, High-fidelity superconducting quantum processors via laser-annealing of transmon qubits, *Sci. Adv.* **8**, eabi6690 (2022).
- [16] A. D. Córcoles, E. Magesan, S. J. Srinivasan, A. W. Cross, M. Steffen, J. M. Gambetta, and J. M. Chow, Demonstration of a quantum error detection code using a square lattice of four superconducting qubits, *Nat. Commun.* **6**, 6979 (2015).
- [17] M. Takita, A. D. Córcoles, E. Magesan, B. Abdo, M. Brink, A. Cross, J. M. Chow, and J. M. Gambetta, Demonstration of Weight-Four Parity Measurements in the Surface Code Architecture, *Phys. Rev. Lett.* **117**, 210505 (2016).
- [18] A. Morvan, L. Chen, J. M. Larson, D. I. Santiago, and I. Siddiqi, Optimizing frequency allocation for fixed-frequency superconducting quantum processors, *Phys. Rev. Res.* **4**, 023079 (2022).
- [19] M. D. Hutchings, J. B. Hertzberg, Y. Liu, N. T. Bronn, G. A. Keefe, M. Brink, J. M. Chow, and B. L. T. Plourde, Tunable Superconducting Qubits with Flux-Independent Coherence, *Phys. Rev. Appl.* **8**, 044003 (2017).
- [20] J. Ku, X. Xu, M. Brink, D. C. McKay, J. B. Hertzberg, M. H. Ansari, and B. L. T. Plourde, Suppression of Unwanted ZZ Interactions in a Hybrid Two-Qubit System, *Phys. Rev. Lett.* **125**, 200504 (2020).
- [21] M. Bal, J. Long, R. Lake, X. Wu, C. R. McRae, H.-S. Ku, J. B. Hertzberg, N. T. Bronn, J. M. Chow, and D. Pappas, Frequency trimming of superconducting fixed-frequency qubits, APS March Meeting 2019..
- [22] M. Carroll, S. Rosenblatt, P. Jurcevic, I. Lauer, and A. Kandala, Dynamics of superconducting qubit relaxation times, (2021), [ArXiv:2105.15201](https://arxiv.org/abs/2105.15201)..
- [23] S. A. Caldwell, N. Didier, C. A. Ryan, E. A. Sete, A. Hudson, P. Karalekas, R. Manenti, M. P. da Silva, R. Sinclair, and E. Acala, *et al.*, Parametrically Activated Entangling Gates Using Transmon Qubits, *Phys. Rev. Appl.* **10**, 034050 (2018).
- [24] N. Didier, E. A. Sete, M. P. da Silva, and C. Rigetti, Analytical modeling of parametrically modulated transmon qubits, *Phys. Rev. A* **97**, 022330 (2018).
- [25] J. M. Gambetta, A. A. Houck, and A. Blais, Superconducting Qubit with Purcell Protection and Tunable Coupling, *Phys. Rev. Lett.* **106**, 030502 (2011).
- [26] S. J. Srinivasan, A. J. Hoffman, J. M. Gambetta, and A. A. Houck, Tunable Coupling in Circuit Quantum Electrodynamics Using a Superconducting Charge Qubit with a V-Shaped Energy Level Diagram, *Phys. Rev. Lett.* **106**, 083601 (2011).

- [27] S. A. J. Hoffman, S. J. Srinivasan, J. M. Gambetta, and A. A. Houck, Coherent control of a superconducting qubit with dynamically tunable qubit-cavity coupling, *Phys. Rev. B* **84**, 184515 (2011).
- [28] G. Zhang, Y. Liu, J. J. Raftery, and A. A. Houck, Suppression of photon shot noise dephasing in a tunable coupling superconducting qubit, *npj Quantum Inf.* **3**, 1 (2017).
- [29] G. Burkard, R. H. Koch, and D. P. DiVincenzo, Multilevel quantum description of decoherence in superconducting qubits, *Phys. Rev. B* **69**, 064503 (2004).
- [30] D. P. DiVincenzo, F. Brito, and R. H. Koch, Decoherence rates in complex Josephson qubit circuits, *Phys. Rev. B* **74**, 014514 (2006).
- [31] A. E. Ruehli, Inductance Calculations in a Complex Integrated Circuit Environment, *IBM J. Res. Dev.* **16**, (1972).
- [32] X. You, J. A. Sauls, and J. Koch, Circuit quantization in the presence of time-dependent external flux, *Phys. Rev. B* **99**, 174512 (2019).
- [33] R.-P. Riwar and D. P. DiVincenzo, Circuit quantization with time-dependent magnetic fields for realistic geometries, *ArXiv:2103.03577*..
- [34] F. Solgun and D. P. DiVincenzo, Multiport Impedance Quantization, *Ann. Phys. (N. Y)* **361**, 605 (2015).
- [35] F. Solgun, D. P. DiVincenzo, and J. M. Gambetta, Simple impedance response formulas for the dispersive interaction rates in the effective Hamiltonians of low anharmonicity superconducting qubits, *IEEE Trans. Microw. Theory Tech.* **67**, (2019).
- [36] A. A. Clerk and D. W. Utami, Using a qubit to measure photon-number statistics of a driven thermal oscillator, *Phys. Rev. A* **75**, 042302 (2007).
- [37] Z. Wang, S. Shankar, Z. K. Mineev, P. Campagne-Ibarcq, A. Narla, and M. H. Devoret, Cavity Attenuators for Superconducting Qubits, *Phys. Rev. Appl.* **11**, 014031 (2019).
- [38] J. M. Gambetta, C. E. Murray, Y.-K.-K. Fung, D. T. McClure, O. Dial, W. Shanks, J. Sleight, and M. Steffen, Investigating surface loss effects in superconducting transmon qubits, *IEEE Trans. Appl. Supercond.* **27**, 1700205 (2017).
- [39] F. C. Wellstood, C. Urbina, and J. Clarke, Low-frequency noise in dc superconducting quantum interference devices below 1K, *Appl. Phys. Lett.* **50**, 772 (1987).
- [40] S. M. Anton, C. Müller, J. S. Birenbaum, S. R. O’Kelley, A. D. Fefferman, D. S. Golubev, G. C. Hilton, H.-M. Cho, K. D. Irwin, and F. C. Wellstood, *et al.*, Pure dephasing in flux qubits due to flux noise with spectral density scaling as  $1/f^\alpha$ , *Phys. Rev. B* **85**, 224505 (2012).
- [41] J. Braumüller, L. Ding, A. P. Vepsäläinen, Y. Sung, M. Kjaergaard, T. Menke, R. Winik, D. Kim, B. M. Niedzielski, and A. Melville, *et al.*, Characterizing and Optimizing Qubit Coherence Based on SQUID Geometry, *Phys. Rev. Appl.* **13**, 054079 (2020).
- [42] J. Bylander, S. Gustavsson, F. Yan, F. Yoshihara, K. Harrabi, G. Fitch, D. G. Cory, Y. Nakamura, J.-S. Tsai, and W. D. Oliver, *et al.*, Noise spectroscopy through dynamical decoupling with a superconducting flux qubit, *Nat. Phys.* **7**, 565 (2011).
- [43] E. Berg, Z. Mineev, A. Kandala, and K. Temme, Probabilistic error cancellation with sparse Pauli-Lindblad models on noisy quantum processors, (2022), *ArXiv:2201.09866*.